Materials Today Bio 24 (2024) 100943

Contents lists available at ScienceDirect

Materials Today Bio

journal homepage: www.journals.elsevier.com/materials-today-bio

Dual-functional 3D-printed porous bioactive scaffold enhanced bone repair by promoting osteogenesis and angiogenesis

Shaorong Li [1], Yutao Cui [1], He Liu, Yuhang Tian, Yi Fan, Gan Wang, Jingwei Wang, Dankai Wu [**], Yanbing Wang [*]

Orthopaedic Medical Center, The Second Hospital of Jilin University, Changchun, 130041, China

ARTICLE INFO

Keywords:
Angiogenesis
Bioactive scaffold
Bone defects
Osteogenesis

ABSTRACT

The treatment of bone defects is a difficult problem in orthopedics. The excessive destruction of local bone tissue at defect sites destroys blood supply and renders bone regeneration insufficient, which further leads to delayed union or even nonunion. To solve this problem, in this study, we incorporated icariin into alginate/mineralized collagen (AMC) hydrogel and then placed the drug-loaded hydrogel into the pores of a 3D-printed porous titanium alloy (AMCI/PTi) scaffold to prepare a bioactive scaffold with the dual functions of promoting angiogenesis and bone regeneration. The experimental results showed that the ACMI/PTi scaffold had suitable mechanical properties, sustained drug release function, and excellent biocompatibility. The released icariin and mineralized collagen (MC) synergistically promoted angiogenesis and osteogenic differentiation *in vitro*. After implantation into a rabbit radius defect, the composite scaffold showed a satisfactory effect in promoting bone repair. Therefore, this composite dual-functional scaffold could meet the requirements of bone defect treatment and provide a promising strategy for the repair of large segmental bone defects in clinic.

1. Introduction

The repair of large segmental bone defects caused by bone tumors, severe trauma, and other diseases has always been a clinical challenge in orthopedics. The blood supply to the bone defect site is typically severely damaged in these scenarios, and bone regeneration ability is relatively insufficient, leading to an increased risk of delayed healing or even bone nonunion [1,2]. At present, the treatment methods commonly used in clinical for bone defects include allografting and autografting [3,4]. However, these methods have some disadvantages. Autografting is limited by the size of the bone defect and may damage the donor site. In comparison, allografting is relatively expensive and can lead to immunological rejection [5,6]. Therefore, it is of great clinical significance to develop a new bone graft that can promote bone regeneration without obvious side effects. In recent years, bone tissue engineering (BTE) has developed rapidly in scientific fields, and has provided a variety of effective treatments for orthopedic diseases. The treatment of large segmental bone defects in clinic is mainly traditional bone grafting, and these methods have certain limitations and disadvantages. Therefore, it is of great clinical significance to develop a bone replacement material with both excellent biological and mechanical properties for the repair of bone defects.

Angiogenesis is crucial for the repair of bone repair. Previous studies have shown that the destruction of local blood supply leads to a significant increase in the incidence of bone nonunion. Local blood supply can provide essential cells and growth factors for bone regeneration, and some special types of vascular endothelial cells, such as type H vascular endothelial cells, can also provide localization signals for osteoblasts [7,8]. Compared with single-function drugs, the dual-functional system with promoting osteogenesis and angiogenesis can promote the repair of bone defects more effectively [9]. Icariin is a flavonoid glycoside isolated from epimedium, confirmed to have the ability to promote osteogenesis and angiogenesis [10]. Therefore, using icariin as a functional molecule to modify the surface of 3D-printed titanium alloy scaffolds is a suitable modification strategy. However, the use of icariin requires a suitable carrier material. Otherwise, the drug is released in a locally explosive manner and causes a localized high concentration, making it difficult for the drug to play a biological role [11].

* Corresponding author.
** Corresponding author. Orthopaedic Medical Center, The Second Hospital of Jilin University, Changchun 130041, China.
E-mail addresses: wudk@jlu.edu.cn (D. Wu), wangyanbing@jlu.edu.cn (Y. Wang).
[1] Shaorong Li and Yutao Cui contribute to this article equally.

https://doi.org/10.1016/j.mtbio.2024.100943
Received 8 October 2023; Received in revised form 20 December 2023; Accepted 2 January 2024
Available online 4 January 2024

The extracellular matrix of bone is mainly composed of collagen fibers and hydroxyapatite (HA) arranged orderly along the former, which is very important for the proliferation of cells and osteogenic differentiation. Hydrogels with extracellular matrix structure in BTE also have obvious positive effects on cell growth and proliferation [12]. However, the degradability and drug release ability of mineralized collagen (MC) cannot match the growth cycle of bone tissue, so it is not suitable for being used as a drug carrier alone. Alginate is a natural linear polysaccharide extracted from oceanic brown algae and the excellent biocompatibility make it become an ideal material for BTE. Alginate combined with mineralized collagen (AMC) can produce exquisite mineralized structure and accelerate the mineralization process of HA on collagen fibers. Alginate can also enhance the mechanical properties and optimize drug release ability of MC by crosslinking with Ca^{2+} to form a coarse fiber network [13]. However, high molecular alginate used in BTE cannot be metabolized *in vivo*, which is not conducive to the growth of bone tissue. Recent studies have found that low molecular weight alginate (25–50 kDa) solves this problem because it has better bioactivity and degradability and keep its basic physical and chemical properties [14]. Therefore, in this study, the improved AMC hydrogel with low molecular weight alginate was used as the loading and sustained release system of icariin.

Simple hydrogel cannot provide enough mechanical support for bone defect, so it is necessary to combine materials with sufficient mechanical strength. In recent years, the development of 3D printing technology has brought about a new strategy for the preparation of bioactive scaffolds in BTE [15]. A variety of materials, such as HA, polylactic acid, polycaprolactone, and many metals, can be used to prepare 3D-printed scaffolds [16,17]. Among these materials, titanium alloy scaffolds have become a common implant in orthopedics because of their good biocompatibility, mechanical properties, and corrosion resistance [18]. Scaffolds with specific size, structural shape, and porosity can be fabricated using 3D printing technology to match and fill the size and shape of bone defects. In addition, titanium alloy scaffolds can provide mechanical support in the bone defect area, improving the stability of bone defect sites and facilitating the growth of bone tissue [19,20]. By

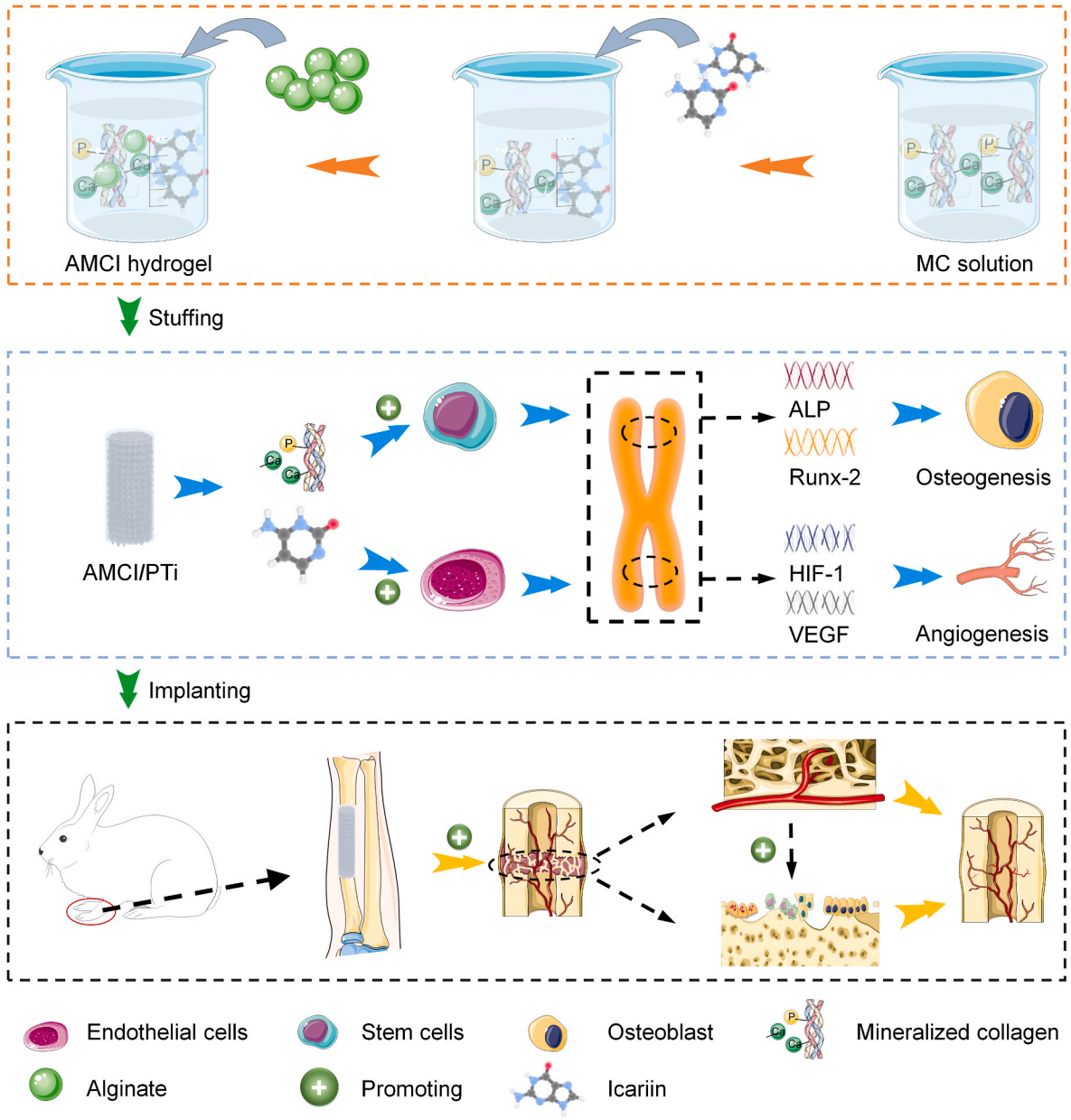

Scheme. 1. Preparation process and biological functional mechanism of the AMCI/PTi scaffold.

designing titanium alloy scaffold with micropore structure, the elastic modulus is similar to that of human cancellous bone, and the problem of stress shielding of implant can be avoided. In addition, the titanium alloy scaffold with microporous structure can not only facilitate the growth of bone tissue, but also enhance the bone formation ability by loading bioactive materials. It is a suitable improvement strategy to combine 3D-printed porous titanium scaffolds with hydrogel to release drugs locally [21].

In this study, a composite dual-functional scaffold capable of promoting bone regeneration and angiogenesis was prepared by combining icariin-loaded AMC hydrogel and a 3D-printed titanium alloy (AMCI/PTi) scaffold (Scheme 1). The *vitro* experiments were performed to study the physicochemical characteristics, drug release process, biocompatibility, osteogenic differentiation, and angiogenic properties of this scaffold. In addition, the AMCI/PTi scaffold was implanted into a large segmental radius defect model to evaluate the effect on bone repair *in vivo*.

2. Materials and methods

2.1. Materials

Ti_6Al_4V powder was purchased from AK Medical Co., Ltd, Beijing, China. Icariin and type I collagen were purchased from Yuanye Bio-Technology Co., Ltd. Shanghai, China. Na_2HPO_4, $CaCl_2$, and NaOH were purchased from Macklin Biochemical Technology Co., Ltd., Shanghai, China. Alginate was purchased from Aladdin Biochemical Technology Co., Ltd, Shanghai, China, and its molecular weight ranged from 25 kDa to 50 kDa. Matrigel was purchased from Corning Incorporated, New York, USA. The well plates used for cell experiments were purchased from Corning Incorporated, New York, USA. The low-glucose DMEM medium, RPMI-1640 medium, fetal bovine serum, penicillin, streptomycin, and 0.25 % EDTA were purchased from Gibco, Grand Island, New York, USA.

2.2. Preparation of AMCI/PTi scaffold

We designed the parameters of the scaffold needed for the experiment by collecting the data of rabbit radius and made the porous titanium alloy scaffold by selective laser melting. The titanium alloy scaffolds used for *in vivo* experiments were long cylinders ($\varphi = 3.5$ mm $\times$ L = 20 mm), and the titanium alloy scaffolds used for *in vitro* experiments were disks ($\varphi = 10$ mm $\times$ L = 3 mm). Other parameters of the titanium alloy scaffolds used in the experiment were as follows: porosity = 75 %, pore size = 600 μm, and strut size = 300 μm. Then, we designed two models of titanium scaffolds and the model data were transferred to a 3D printer (Stratasys, Eden Prairie, MN) to print these scaffolds used Ti_6Al_4V powder with the average particle diameter of 15–45 μm. The laser power, scanning speed and layer thickness were 90 W, 700 mm/min and 25 μm respectively. The process of scaffold printing was carried out in high-purity argon atmosphere and the oxygen was kept below 80 ppm. All the prepared titanium alloy scaffolds were ultrasonically cleaned in acetone, ethanol and deionized water for 60 min three times, and then the scaffolds were autoclaved at 121 °C for 20 min. The scaffolds were put into a constant temperature oven at 60 °C to dry, and then they were taken out and exposed to ultraviolet light.

In this study, the AMC hydrogel was prepared using biomimetic mineralization. First, type I collagen was dissolved in acetic acid (0.3 M) to form a solution (7 mg/mL). Then, Na_2HPO_4 (1.2 M) solution and icariin were added to the collagen solution. The final concentrations of PO_4^{3-} and icariin were 20 mM and 1 nM, respectively. The appropriate amount of $CaCl_2$ (2 M) solution was added to attain a Ca/P ratio of 1.67. After stirring the mixed solution, the appropriate amount of NaOH solution was added to bring the pH value to between 7.35 and 7.45. The prepared titanium scaffold was added into the collagen solution after cleaned by ultrasonic and sterilization. Then, sodium alginate was added to the mixture to stimulate the formation of AMC hydrogel, and the weight ratio of alginate/collagen was 1:1. After stirring evenly, the mixed solution formed hydrogel and the AMCI/PTi scaffold was finished. In addition, the 3D-printed titanium alloy scaffolds filled with AMC hydrogel (AMC/PTi) without icariin were prepared using the same protocol as the control group.

2.3. Characterizations of AMCI/PTi scaffold

After sputtering gold, the surface micropore structure of the scaffold was observed by SEM (Hitachi, Hitachi SU-8100, Japan) at an accelerated voltage of 20 kV, and the magnification was 50–20,000 times. Then EDS (FEI, TECNAI G2 F30, USA) was used to determine the chemical composition of the AMCI/PTi scaffold and the element distribution on the surface of the scaffold. In addition, the chemical structure of the AMCI/PTi scaffold was analyzed using a Fourier transform infrared spectrometer (NICOLET380, Boston, MA, USA), and the wavenumber range was 4000–400 cm^{-1}.

To evaluate the viscoelastic behavior of the AMC with icariin (AMCI) hydrogel, rheological tests were performed using a Kinexus Lab + rheometer (Netzsch, Bavaria, Germany) with a parallel plate geometry (25 mm diameter, 1.0 mm gap) at 25 °C. In the stress detection mode, the angular velocity was set at 6.28 rad/s, and the frequency was 1 Hz. The hydrogel storage modulus (G') and loss modulus (G'') were measured in the range of shear strain between 0.1 % and 300 %. In the shear rate mode, the temperature was set at 25 °C, and the shear viscosity and shear stress of the hydrogel were measured in the shear rate range of 0.1–1000 s^{-1}.

The mechanical properties of the AMCI/PTi scaffold were measured by universal testing machine (Instron 5567, Instron Ltd., USA). The compression test was carried out according to the ISO13314:2011 standard, and the universal testing machine tested at a constant speed of 1 mm/min until there was no more displacement. The compressive strength and the elastic modulus of the scaffold were calculated by the obtained stress-strain curve.

2.4. Degradability of the AMCI hydrogel

The degradability and biocompatibility of the AMCI hydrogel *in vivo* were evaluated. All animal experiments were performed under the authorization of the Animal Care and Experiment Committee at Jilin University, following the international standards on animal welfare (Approval No.151, date of approval: 2022). Six-week-old Sprague–Dawley rats were selected as experimental animals and anesthetized using 2 % isoflurane after depriving them of food and water. Each rat was injected with 0.5 g of AMCI hydrogel (W_a) at the same location on its back. The rats were randomly divided into 10 groups, each group containing three rats. The rats were sacrificed at specific times of 0, 4, 7, 10, 14, 21, 28, 35, 42, and 49 days, and the remaining hydrogel was taken out and weigh (W_t). The degradation rate of AMCI hydrogel was calculated according to the weight of residual hydrogel. The degradation rate formula is as follows:

$$\text{Degradation ratio}(\%) = (W_a - W_t)/W_a \times 100\%$$

In addition, the skin tissue near the hydrogel was retained and fixed in a 4 % paraformaldehyde solution. Then, hematoxylin-eosin (HE) staining was performed to observe the changes in skin tissue.

2.5. Drug release assay in vitro

The AMCI/PTi scaffold was immersed in 5 mL PBS solution (Solar, Beijing, China) to determine the icariin release curve. At specific times, including 1, 7, 14, 21, and 28 days, the scaffolds were transferred and placed in another 5 mL fresh PBS solution. The remaining liquid was collected, and the absorbance was determined using an ultraviolet

spectrophotometer (Lambda800, PerkinElmer, USA) at 270 nm.

2.6. In vitro experiments

2.6.1. Cell viability, proliferation, and morphology

Bone mesenchymal stem cells (BMSCs) were isolated from 1-week-old New Zealand white rabbits. The BMSCs were subsequently cultured in a low-glucose-DMEM medium containing 10 % fetal bovine serum and 1 % penicillin and streptomycin. The culture environment was an incubator at 37 °C and 5 % CO_2 (Thermo Fisher Scientific, Shanghai, China). In this study, third-generation BMSCs were used for subsequent cell experiments.

The compatibility of the AMCI/PTi scaffolds was detected using a Calcein-AM/PI Double Stain Kit (BestBio, Shanghai, China). The BMSCs were seeded in 24-well plates at a density of 6×10^3 cells/well and cultured with empty control (CON), empty porous titanium alloy scaffolds (PTi), AMC/PTi, and AMCI/PTi scaffolds for 1 and 3 days, respectively. For the Calcein-AM/PI staining experiments, the Calcein-AM/PI staining solution was prepared according to the manufacturer's instructions. The BMSCs were cultured with Calcein-AM/PI staining solution in the dark, and the staining solution was removed from plates after 15 min. The results were observed under a fluorescence microscope after washing the plates with PBS (Olympus Corporation, Japan).

A Cell Counting Kit 8 (Beijing solarbio science&technology Co., ltd, China) was used to determine the proliferation rate of BMSCs on day 1, 3, and 7. The BMSCs were seeded in 24-well plates at a density of 6×10^3 cells/well and cultured with CON, PTi, AMC/PTi, and AMCI/PTi scaffolds for 1, 3, and 7 days, respectively. The BMSCs were incubated with 100 μL of CCK-8 solution for about 3 h in the dark. After collecting the supernatant, the absorbance was measured at 450 nm using a microplate reader (Thermo Fisher Scientific, Shanghai, China).

The morphology of BMSCs in each group on day 3 was observed using F-actin/DAPI staining (Beijing Solarbio Science & Technology Co., Ltd, China). The BMSCs were seeded in 24-well plates at a density of 6×10^3 cells/well in the CON, PTi, AMC/PTi, and AMCI/PTi groups, and the medium was removed after culturing for three days. The plates were rinsed with PBS solution to remove the remaining medium and then fixed with 4 % paraformaldehyde for 15 min. Phalloidin solution (5 μg/mL) was added to the plates and incubated for 30 min. After removing the phalloidin staining solution and rinsing it with PBS, the BMSCs were incubated in DAPI solution with a dilution of 1:1000 for 5 min in the dark. After removing the DAPI staining solution and rinsing with PBS, the staining results were observed and photographed under a fluorescence microscope, and the length of the cell microfilament was analyzed using ImageJ software (NIH, Bethesda, MD).

2.6.2. Alkaline phosphatase (ALP) activity assay

The BMSCs were seeded at 6×10^3 cells/well in 24-well plates with CON, PTi, AMC/PTi, and AMCI/PTi scaffolds at 37 °C and 5 % CO_2. After the BMSCs adhered to the plate, 50 mM ascorbic acid (Sigma-Aldrich, USA), 10 mM β-glycerophosphoric acid (Sigma-Aldrich, USA), and 100 nM dexamethasone (Sigma-Aldrich, USA) were added to each group. After culturing each group for 7 and 10 days, ALP staining was performed to evaluate the osteogenic differentiation ability. Each sample was rinsed three times with PBS and fixed with 4 % paraformaldehyde for 15 min. ALP chromogenic reagent was added to incubate for 30 min and observed under a microscope. In addition, Alkaline Phosphatase Activity Detection Kits (Beyotime Biotechnology, Shanghai, China) were used to detect the activity of ALP. The BMSCs in each group were rinsed three times with PBS before staining and then lysed with cell lysis buffer (Beyotime Biotechnology, Shanghai, China) on ice. According to the manufacturer's instructions, a set amount of standard product, substrate, and sample were added to the blank plate and the reaction was carried out at 37℃ for 30 min. The optical density (OD) value of each group under 405 nm irradiation was measured after incubating for approximately 30 min. The ALP activity of each group was calculated, and each group was tested in triplicate.

2.6.3. Cell migration and tube formation assay

The effects of different scaffolds on the migration of human umbilical vein endothelial cells (HUVECs, Guangzhou Cellcook Biotech Co., Ltd., China) were detected using wound healing and tubule formation assays, respectively. The CON, PTi, AMC/PTi, and AMCI/PTi scaffold groups were placed in RPMI-1640 medium without cells for 1 day, and the leaching solution in each group was collected. Matrigel was coated in 96-well culture plates at a low temperature and then incubated at 37 °C for 30 min to solidify into a hydrogel state. The HUVECs were seeded at 2×10^4 cells/well into 96-well plates and cultured with 150 μL leaching solution for 6 h. Calcein was used to stain cells to make the results easier to observe. The tubular structures of HUVECs were observed and photographed using an inverted microscope. ImageJ software was used to count the tube branch points for evaluating the angiogenic ability in each group.

The HUVECs were seeded at 2×10^4 cells/well in 6-well plates and cultured in RPMI-1640 medium containing 10 % fetal bovine serum and 1 % penicillin and streptomycin (Gibco, Grand Island, NY, USA). Then, scratches were prepared using a 200 μL pipette tip when the HUVECs filled the plates, and the HUVECs were cultured with a leaching solution after being washed with PBS. The medium was discarded after incubating for 1 day, and the results were observed using a microscope. ImageJ software was used to count the healing area for evaluating angiogenic ability.

2.6.4. Real time-quantitative polymerase chain reaction (RT-qPCR)

The HUVECs were seeded in 6-well plates at 2×10^4 cells/well with CON, PTi, AMC/PTi, and AMCI/PTi scaffolds at 37 °C and 5 % CO_2. After culturing for 2 days, an RT-qPCR assay was performed to detect the expression of VEGF, BFGF, and HIIF-1 in HUVECs. The total RNA was extracted using a SPARK Easy Cell RNA Kit (Sparkjade, Shandong, China), and genomic DNA clearance and reverse transcription were performed using a StarScript II RT Kit (Genestar, Beijing, China). Then, the amplification process was performed using a StarScript II One-step RT-qPCR Kit (Genestar, Beijing, China). The relative gene expressions were calculated via the $2^{-\Delta\Delta Ct}$ method by normalizing with a housekeeping gene. In addition, the BMSCs were seeded at 6×10^3 cells/well in 24-well plates and cultured in an incubator at 37 °C and 5 % CO_2. After the BMSCs adhered to the plate, 50 mM ascorbic acid, 10 mM β-glycerophosphoric acid, and 100 nM dexamethasone were added to each group. The expression levels of Runx-2, osteocalcin (OCN), and ALP in BMSCs were detected using the above methods after culturing for 14 days. The sequence of primer fragments used in the experiment is shown in Table A1.

2.7. Animal experiments in vivo

2.7.1. Preparation of large segmental radius defect model

All animal experiments were performed under the authorization of the Animal Care and Experiment Committee at Jilin University, following the international standards on animal welfare (Approval No.151, date of approval: 2022). Eighteen female New Zealand white rabbits (2-month-old) were selected to establish the large segmental radius defect model. A radius osteotomy was performed to establish the radius defect model. The New Zealand white rabbits were randomly divided into three groups, and anesthetized by injection of 3 % sodium pentobarbital (50 mg/kg) at the ear marginal vein. A 2 cm sagittal incision was made on the right foreleg, and the radius was exposed layer-by-layer. After the periosteum of the osteotomy area was removed, a 2 cm radius segment was cut using a sterilized bone saw. The blood and bone fragments at the bone defect by osteotomy was cleaned up and the bone defect area was filled with empty titanium alloy scaffolds, AMC/PTi, and AMCI/PTi scaffolds, respectively. By adjusting the two ends of the scaffold to correspond to the broken end of bone defect, each group

of scaffolds can be properly embedded in the bone defect. After filling the bone defect with the above-mentioned scaffolds, the incision was closed layer-by-layer. Because of the special fusion relationship between ulna and radius in rabbits, ulna can be used as an internal fixator for radius defect. Therefore, the implanted scaffold can be effectively fixed only by the tension generated by suturing soft tissue and the broken bone [22]. Penicillin (1.5 mg/kg) was used within three days after the operation to avoid infection. The New Zealand white rabbits were killed at twelve weeks after the operation, and the specimens were fixed in a 4 % paraformaldehyde solution for subsequent experiments. The images of intraoperative surgery are shown in Figure A1.

2.7.2. X-ray

Digital radiographs were performed immediately after the osteotomy operation under anesthesia using an X-ray machine (AMX4, GE Healthcare, Buckinghamshire, UK). The peak voltage, current and radiation dose were 250 kVP, 16 mA and 5Gy, respectively. In addition, the area of bone defects was examined at 12 weeks after the operation.

2.7.3. Micro-CT

The area of bone defects was examined using micro-CT (SkyScan 1076 scanner, Kontich, Belgium) at 12 weeks after the operation. The pixel size of the image acquisition, the voltage, and the current were 18.26 μm, 48 kV, and 200 mA, respectively. The micro-CT images were constructed into a three-dimensional image, and the scanning area was where the scaffolds were located. Then, a CT Analyzer (SkyScan 1076 scanner, Kontich, Belgium) was used to quantitatively calculate the percentage of bone volume to tissue volume (BV/TV), bone mineral density (BMD), trabecular bone number (Tb.N) and trabecular bone thickness (Tb.Th) in each group.

2.7.4. Histological analysis

The bone regeneration at the defect site was analyzed using Masson staining and Van–Gieson staining. The rabbit radius were collected at 12 weeks after the operation, and the specimens were fixed in a 4 % paraformaldehyde, embedded in paraffin, and made into hard tissue sections at a thickness of 30 μm without decalcification. Then, the Masson staining and Van–Gieson staining were performed. A digital microscope (DSX 500; Olympus Corporation, Tokyo, Japan) was used to observe the bone repair, and the area of the new bone was calculated using Image J software for semi-quantitative analysis.

2.7.5. Immunohistochemistry

The relative expressions of CD31, HIF-1, Runx-2, and OCN in new bone tissue at the bone defect site were detected using immunohistochemical staining to evaluate osteogenesis in each group. The bone tissue around the scaffolds was collected at 12 weeks after the operation. The specimens were fixed in a 4 % paraformaldehyde, decalcified in 10 % EDTA for 3 weeks, embedded in paraffin, and sectioned at a thickness of 5 μm. Then, the sections were incubated with the CD31, HIF-1, Runx-2, and OCN antibodies (Bioss Biotechnology Co., Ltd., Beijing, China) overnight at 4 °C. The secondary antibody used for staining was goat anti-rabbit immunoglobulin G conjugated to horseradish peroxidase (Servicebio Technology Co., Ltd., Wuhan, China). After incubation with the secondary antibody, the number of CD31-positive, HIF-1-positive, Runx-2-positive, and OCN-positive cells were observed and counted under a light microscope.

2.8. Statistical analysis

All data in this experiment were expressed as mean ± standard deviation for $n \geq 3$. Statistical analysis was carried out using a one-way analysis of variance with Turkey's test. $p < 0.05$ was considered statistically significant. Statistical differences were expressed as * ($p < 0.05$), ** ($p < 0.01$), and *** ($p < 0.001$). All data were analyzed using SPSS 22.0 analysis software (SPSS Inc., Chicago, USA).

3. Results and discussion

3.1. Characterizations of the AMCI/PTi scaffold

The AMC and AMCI hydrogel prepared at room temperature can be seen clearly in Fig. 1A. The AMCI hydrogel can be prepared at room temperature, and the addition of icariin had no obvious effect on hydrogel formation. In this study, two kinds of titanium porous alloy scaffolds made using 3D printing technology are shown in Fig. 1B, in which the disk-shaped scaffold was used for *in vitro* experiments, and the cylinder-shaped scaffold was used for *in vivo* experiments. The shape and size of the scaffold used *in vivo* experiments depended on the anatomical data of rabbit radius, and the shape of the scaffold used *in vitro* experiments was based on our previous research design.

The SEM images showed the pores of the porous scaffolds were uniform, and the average pore size was 600 μm (Fig. 1C). For titanium alloy microporous scaffold, the ideal osseointegration effect may be achieved when the pore size is 300–500 μm and the porosity is about 75–90 % [22]. In this study, the pore size and porosity of the titanium scaffold was 600 μm and 75 % respectively. The pore size of the scaffold was slightly increased in order to provide enough space for loading AMCI hydrogel. This porosity and pore size of the scaffold have been studied and used many times, and it was suitable for loading hydrogel and bone ingrowth [23]. As shown in the images, AMCI hydrogel was able to fill the pore interior of the titanium alloy scaffold uniformly to achieve hydrogel loading with icariin. And HA crystal was uniformly attached to collagen fibers in the mineralization process and crosslinked with alginate to form hydrogel. This can strengthen the internal fiber network and enhance the mechanical strength and stability of the hydrogel.

Fig. 1D showed the Fourier infrared spectra results of the AMCI/PTi scaffold. In the results, the absorption peaks at 2972 and 1634 cm^{-1} were representative of the classical structure of collagen. This indicated that the helical structure of collagen was not damaged during the preparation process. The absorption peaks at 1634 and 1414 cm^{-1} were attributable to the stretching vibrations of asymmetric and symmetric COO^{-} groups in alginate. In addition, the absorption peaks detected at 1031 and 524 cm^{-1} indicated the presence of an HA. The absorption peaks at 2929 and 1089 cm^{-1} confirmed the presence of icariin in the ACMI/PTi scaffold. The above results indicated the presence of HA, collagen, alginate, and icariin in the composite scaffold, and these structures were intact to ensure normal function.

The viscoelastic behavior of AMCI hydrogel was studied using rheological experiments (Fig. 1E). The results showed that G′ and G″ were independent of the applied shear strain between 0.1 % and 300 %. G′ represented the energy stored in the elastic structure of the sample and is usually related to the strength of the material [24]. It was found that the intersection of G′ and G″ for the hydrogel occurs at about 20.03 % strain, which indicated that the AMCI hydrogel was in a stable gel state when the shear strain was less than 20.03 % and G′ is higher than G". When the shear strain was higher than 20.03 %, the G′ is lower than the G″ and the AMCI hydrogel transformed into the sol state. Moreover, the viscoelastic properties of the AMCI hydrogel were not affected under low shear strain, which ensured the stability of the AMCI hydrogel in the titanium alloy scaffold. The relationship between the shear viscosity and the shear rate of the AMCI hydrogel is shown in Fig. 1F. The shear viscosity of the hydrogel decreased with an increase in shear rate, indicating that the AMCI hydrogel exhibited shear thinning behavior. When the shear rate increased, the disordered polymer chain of the AMCI hydrogel was arranged into an organized structure according to the flow direction. This property of shear thinning is consistent with the mechanical characteristics of non-Newtonian fluids, which is an important feature of the injectable properties of hydrogels [25]. This meant that when suitable stress was applied to the AMCI hydrogel, it can flow smoothly and match irregular bone defects. In addition, this result was consistent with amplitude scanning tests that showed the viscosity

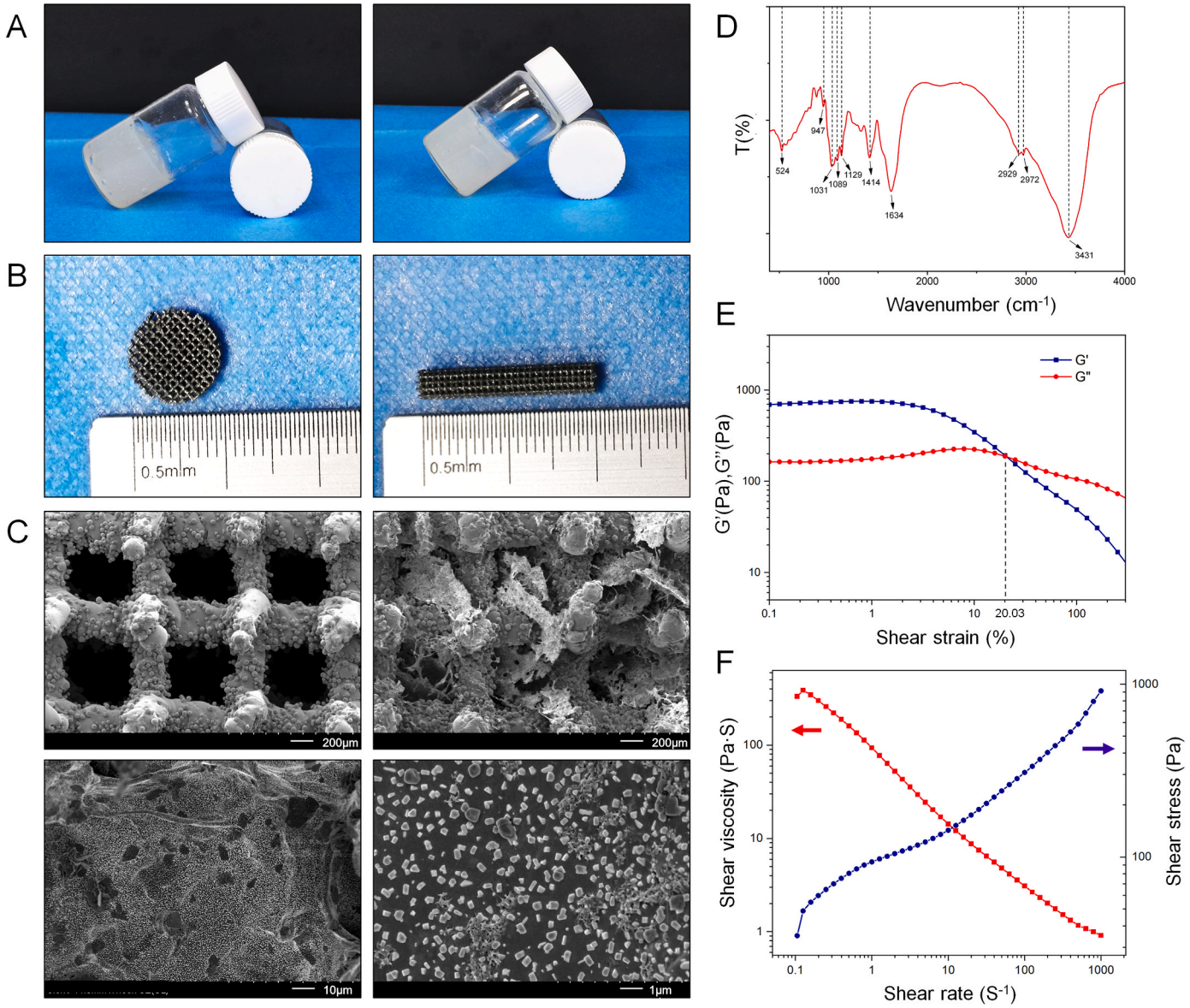

Fig. 1. The characterizations of the AMCI/PTi scaffold. (A) The images of AMC (left) and AMCI (right) hydrogel. (B) The images of titanium alloy scaffolds used *in vitro* (left) and *in vivo* (right) experiment (the minimum scale of the ruler was 0.5 mm). (C) The scanning electron microscope images of the titanium alloy and AMCI/PTi scaffold. (D) The results of infrared spectroscopy detection for the AMCI/PTi scaffold. (E) G′ and G″ of AMCI hydrogel varied with shear strain. (F) The plot of shear stress and viscosity against shear rate for AMCI hydrogel.

modulus of the AMCI hydrogel decreased when the shear stress increased gradually.

The element deposition and distribution on the surface of AMCI/PTi scaffold were further analyzed by EDS. Fig. 2A and B showed the distribution of elements C, O, Na, P, Ca, and Ti and the element ratio on the surface of the AMCI/PTi scaffold. These elements were distributed in different components of the hydrogel, and these was evenly distributed on the surface of titanium scaffold, which showed that all components in AMCI/PTi scaffold are evenly distributed and the AMCI hydrogel was evenly covered on the surface of scaffold. This was beneficial to the stable degradation of hydrogel and the uniform release of drugs, and also provided a suitable interface for the adhesion of BMSCs and the growth of new bone tissue.

Fig. 2C showed the elastic modulus of the two groups of scaffolds and the ultimate compressive strength, which was the maximum stress that the scaffold bear before being destroyed. The compressive strength of titanium scaffold and AMCI/PTi scaffold were 43.95 ± 3.00 and 47.41 ± 4.36 MPa, respectively, and there was no obvious difference between the two groups. The elastic modulus of titanium scaffold and AMCI/PTi scaffold were 1.66 ± 0.22, 1.57 ± 0.08 GPa, respectively, and there was no obvious difference between the two groups. This showed that the addition of AMCI hydrogel had no obvious effect on the mechanical properties of titanium scaffold. The elastic modulus of the scaffold was similar to that of human cancellous bone to avoid the stress shielding phenomenon to the surrounding bone tissue at the bone defect [26]. The compressive strength of the scaffold was between human cortical bone and cancellous bone, so it can play a sufficient supporting role for cancellous bone defect. Moreover, AMCI/PTi scaffold need to combine with some internal fixation devices to provide enough mechanical support for cortical bone defects.

3.2. Degradability and drug release

The degradation process of the AMCI hydrogel was shown in Figure A2A. It showed that the subcutaneous hydrogel mass gradually became smaller, and there was no obvious inflammatory reaction on the

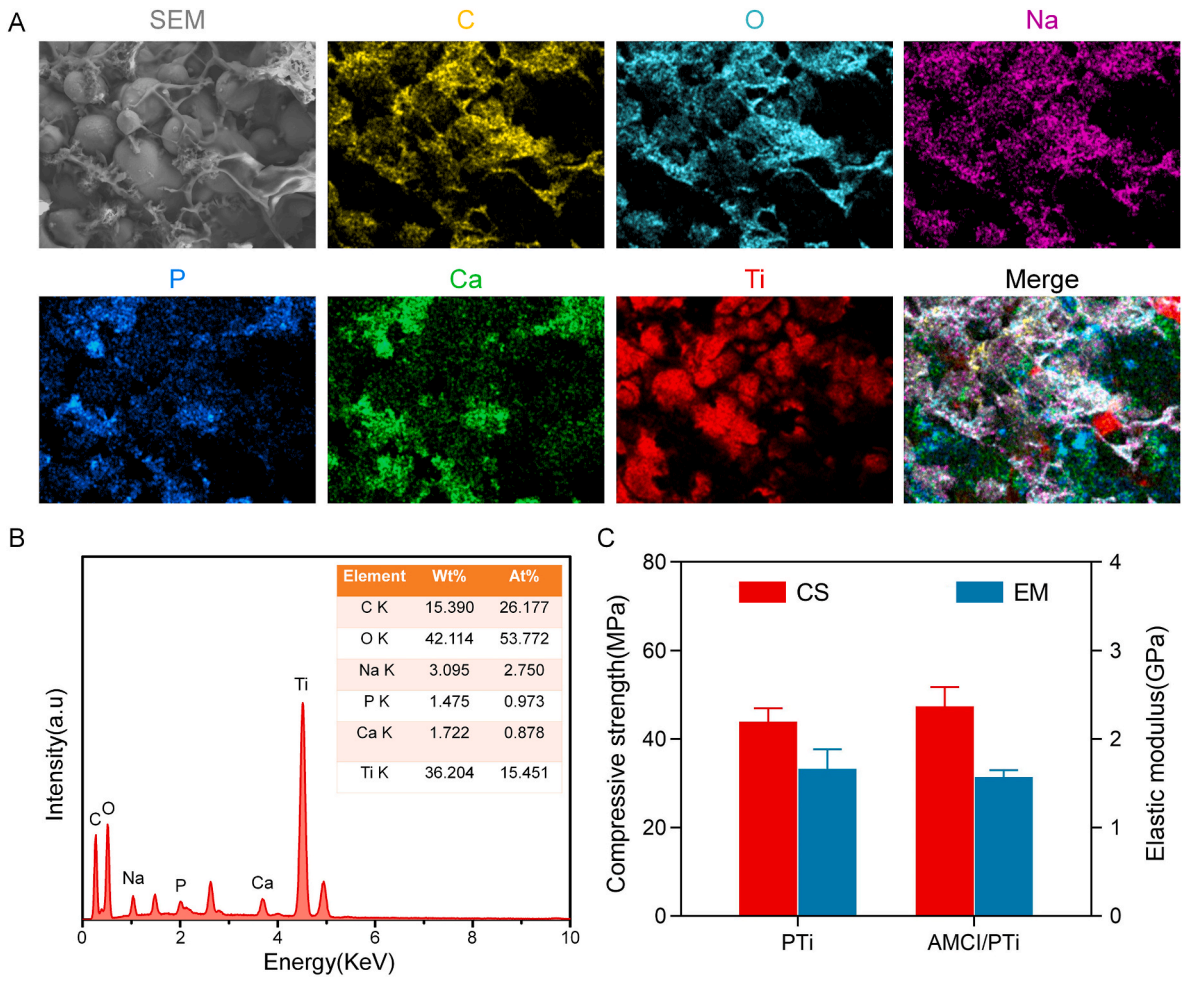

Fig. 2. EDS analysis and compressive strength detection of AMCI/PTi scaffold. (A) Element distribution diagram on the surface of AMCI/PTi scaffold (B) Element ratio on the surface of AMCI/PTi scaffold (C) Comparison of compressive strength and elastic modulus between Ti scaffold and AMCI/PTi scaffold (CS and EM in the diagram represent compressive strength and elastic modulus respectively).

skin surface on day 0, 14, 28, and 42. The degradation curve of the AMCI hydrogel was shown in Figure A2B. The initial weight of the hydrogel was 0.50 ± 0.01 g, and the weight on day 42 was 0.20 ± 0.01 g. The degradation rate decreased relatively from day 0 to day 42. The residual hydrogel weight was 0.17 ± 0.06 g on day 49, and the degradation curve was nearly flat after 49 days. This indicated that the AMCI hydrogel was mostly not further degraded after 49 days.

The AMCI hydrogel consisted mainly of alginate, type I collagen fibers, HA, and icariin. Due to the lack of related hydrolytic enzymes, alginate with high molecular weight may not be fully degraded in physiological systems or removed from the body, which limits its application in biomedicine [27]. This study showed that the depolymerized alginate obtained good bioactivity and degradability by reducing the molecular weight compared with high molecular weight alginate [28]. The degradation rate of alginate in the body was increased upon reducing the size of the alginate chain after depolymerization, and the space for bone tissue growth is provided [14]. Type I collagen also has good degradability, but the degradation rate of HA is very slow, which was one of the reasons for the incomplete degradation of the AMCI hydrogel [29,30]. After 56 days, the degradation rate of AMCI hydrogel was 65.56 ± 1.39 %, which was the ratio of collagen, alginate and HA metabolized *in vivo*, and the content of HA in the initial AMCI hydrogel was 38.41 % by calculation. It was calculated from the ratio of the mass of HA added to the total mass of the hydrogel when preparing the AMCI hydrogel. Due to HA was difficult to be degraded, the main component of the residue was HA, and there were also a small amount of collagen and alginate [31,32]. Although the hydrogel remained *in vivo*, a small amount of hydrogel did not affect the growth of bone tissue. In addition, the main components of the residue were HA, a small amount of alginate and collagen. These materials all have good compatibility and will not have side effects on local tissue. And the remaining HA and collagen fibers also have a positive effect on the process of bone defect repair.

In this study, we chose 10^{-6} mol/L as the loading concentration of icariin. Previous studies have shown that excessive icariin will inhibit osteogenesis, and 10^{-6} mol/L was a more suitable choice for the treatment to bone defect in BTE. Icariin at this concentration not only has strong osteogenic activity, but also can promote angiogenesis [33]. Figure A2C showed the drug release curve of AMCI/PTi *in vitro*. The release rate on the first day was 24.83 ± 2.00 %, and the cumulative release rate on day 21 was 76.03 ± 0.90 %. In the process of release, with the speed gradually decreasing, and the cumulative release of icariin basically reached a maximum value of 77.23 % ± 0.90 % on day 28.

The drug in hydrogel was mainly released by way of free diffusion and the degradation of hydrogel [34]. The drug was mainly released through free diffusion at the early stage of the release process because the degradation of the hydrogel was not obvious. The drug located on the surface of the hydrogel more easily diffused into the microenvironment, especially on the first day, resulting in an initial burst release. After the drugs outside the hydrogel were released by diffusion, others inside the hydrogel were released mainly through the degradation of the

hydrogel. Therefore, the degradation rate of the hydrogel was key to controlling the slow release of the drugs. The network formed upon HA crosslinking with alginate reduced the degradation rate of the AMCI hydrogel and prolonged the release of icariin. The release rate of icariin in the second week slowed significantly compared with the first week, indicating the slow-release property of the AMCI hydrogel. Finally, the release rate of icariin gradually decreased with a decrease in the AMCI hydrogel degradation rate, and the maximum release of icariin into solution was basically reached on day 28.

For the drug delivery system in BTE, a stable drug release process is particularly important. In conclusion, the release process of icariin was stable and continuous and this indicated that the AMCI/PTi scaffold could release icariin steadily and ensure the appropriate release period in a localized manner. The fast degradation rate of MC leads to a too-fast drug release rate, according to a previous study. Alginate can not only assist the mineralization process of collagen but also form a denser fibrous network with Ca^{2+} to slow hydrogel degradation [35,36]. Therefore, the release of icariin from the AMCI/PTi scaffold was a suitable and ordered process. In addition, it is also important whether the period of drug release can cover the critical period of bone regeneration, especially for the early stage of bone growth. The released icariin can activate the osteogenesis-related factors produced to enhance osteogenesis, and these factors can also activate other reactions to have a long-term impact on the subsequent bone tissue repair and reconstruction. Although the drug was basically released after 28 days, the hydrogel continued to degrade at this time. Collagen and HA produced by hydrogel degradation also had certain positive effects on the later bone defect repair.

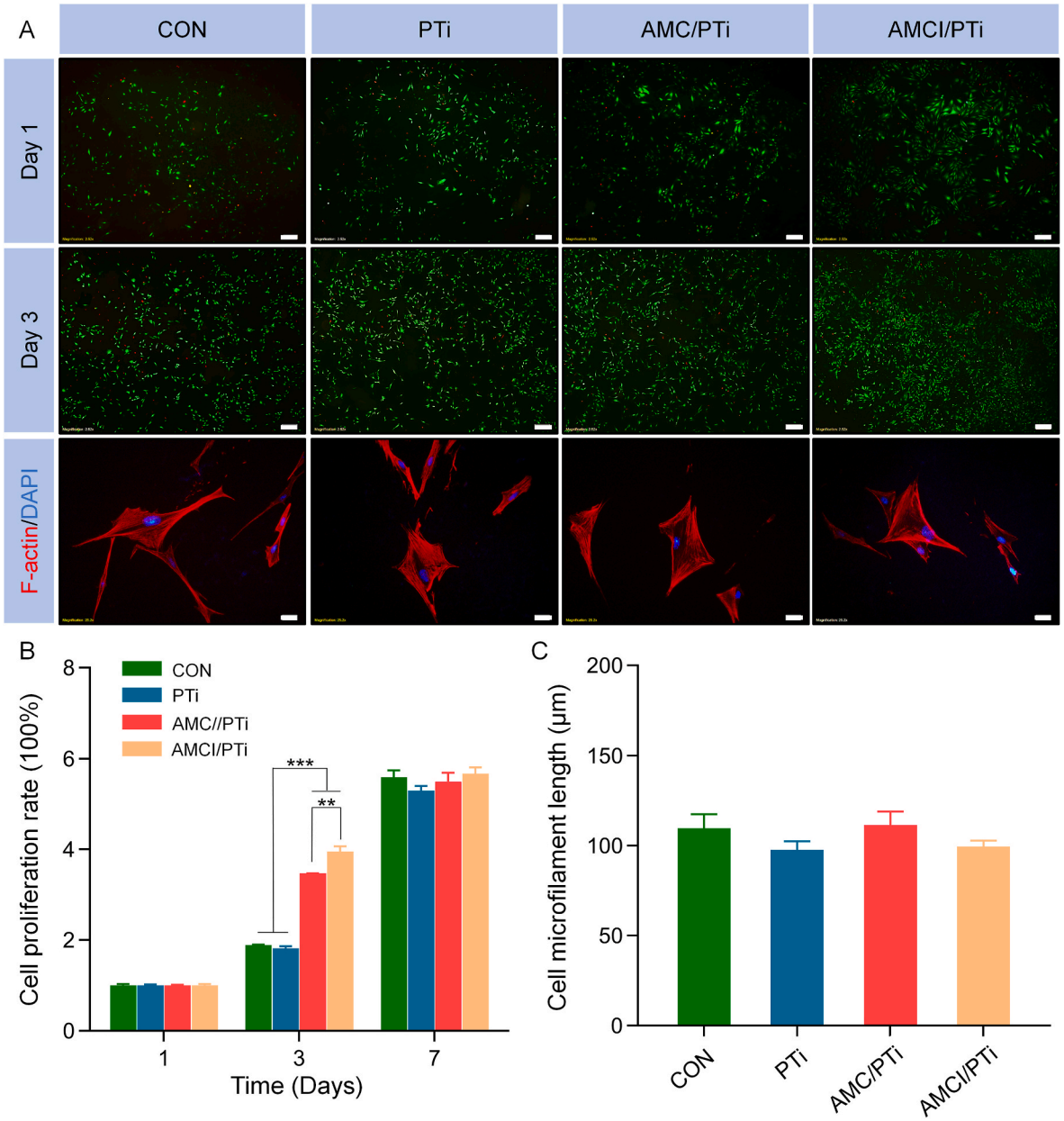

Fig. 3. The effect of scaffolds on the proliferation and morphology of BMSCs. (A) The Calcein-AM/PI and F-actin/DAPI staining of each scaffold. The scales of the images were 200 μm (Calcein-AM/PI staining) and 20 μm (F-actin/DAPI staining). (B) The cell proliferation rate of each group on day 1, 3, and 7. (C) The cell microfilament length of BMSCs of each group in F-actin/DAPI staining on day 3. (n = 3, *indicates significant differences between groups, *$p < 0.05$; **$p < 0.01$, ***$p < 0.001$, the quantitative analysis of F-actin staining was that all samples in three groups of repeated experiments in each group were taken by five-point sampling method and the cell microfilaments are counted.).

3.3. Effects on cell viability, proliferation, and morphology

The biocompatibility of the AMCI/PTi scaffold was evaluated according to Calcein-AM/PI staining (Fig. 3A). The results of Calcein-AM/PI staining showed that the CON, PTi, AMC/PTi, and AMCI/PTi groups had no obvious cytotoxicity on day 1 and 3. Compared with day 1, the living cells increased in each group on day 3. This indicated that the scaffolds in each group all had good biocompatibility.

According to the results of the CCK-8 assay (Fig. 3B), the cell proliferation rates of the CON, PTi, AMC/PTi, and AMCI/PTi groups showed

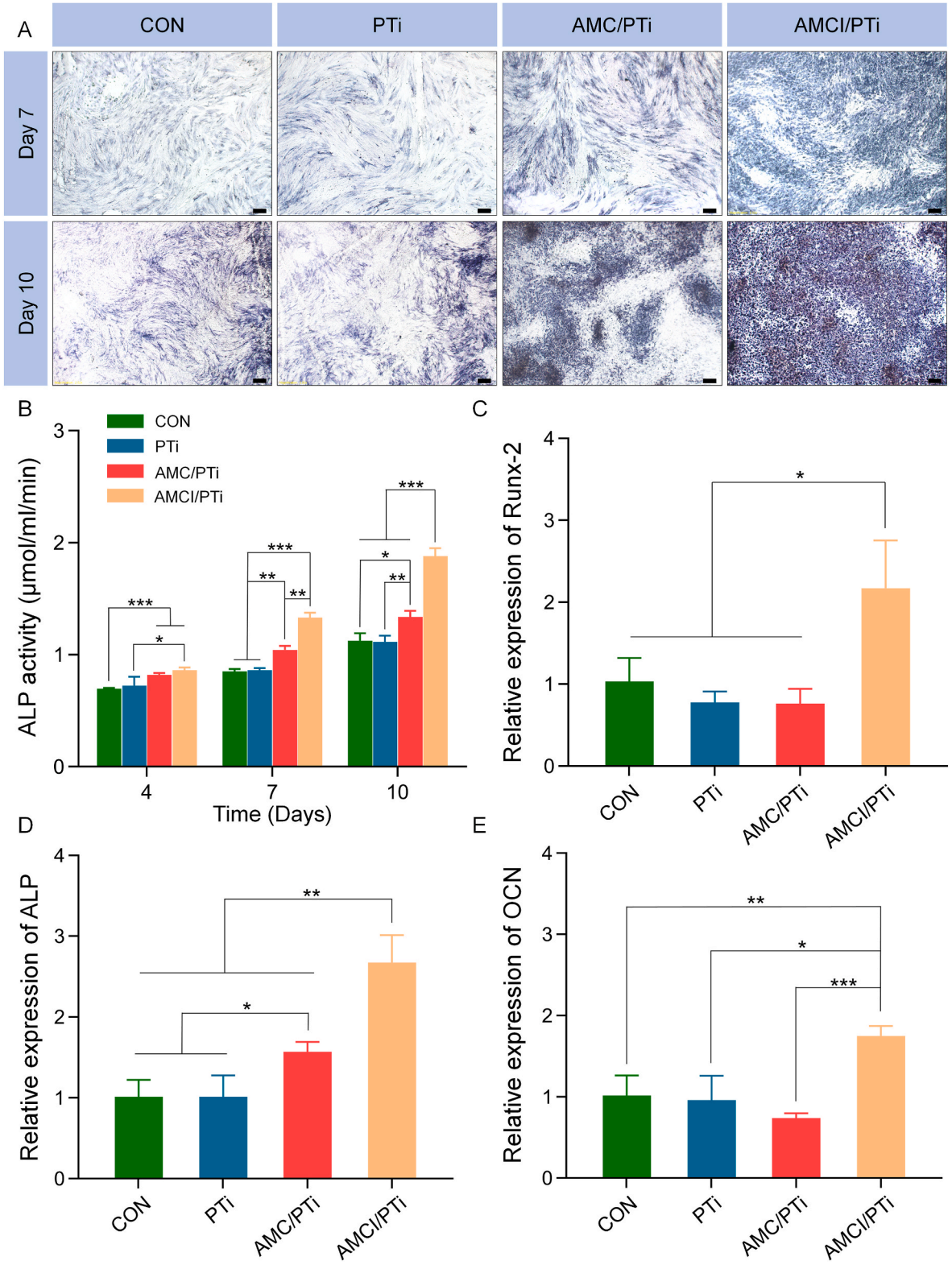

Fig. 4. The effect of each group on BMSCs osteogenic ability. (A) The ALP staining images of each group on day 7 and day 10. The scale of the images was 200 μm. (B) The ALP activity detection of each group on day 4, 7, and 10 (C, D, E). The relative mRNA expression of Runx-2, ALP, and OCN in each group on day 14. (n = 3, *indicates significant differences between groups, *p < 0.05; **p < 0.01, ***p < 0.001).

no significant difference among the four groups on day 1. However, on day 3, the proliferation rates of the CON, PTi, AMC/PTi, and AMCI/PTi groups were 1.88 ± 0.02, 1.82 ± 0.03, 3.47 ± 0.01, 3.95 ± 0.11, respectively. The cell proliferation rates of the AMC/PTi and AMCI/PTi groups were significantly higher than in the CON and PTi groups ($p < 0.001$), and the cell proliferation rate of the AMCI/PTi group was higher than in the AMC/PTi group ($p < 0.01$). This showed that AMC/PTi and AMCI/PTi scaffolds can effectively promote the proliferation of BMSCs. Studies have shown that both MC and icariin can promote the proliferation of BMSCs. Icariin can induce ERK and p38 phosphorylation, and significantly up-regulate the expression of ELK1 and c-MYC of MAPK pathway. MAPK pathway plays an important role in regulating cell proliferation, and icariin can enhance the proliferation of BMSCs by activating MAPK pathway [37]. In addition, Xuan et al. found that MC can also promote the proliferation of BMSCs, which was related to the expression of proliferation-related genes in BMSCs [38]. The AMCI/PTi group had a more significant effect than any other group. This showed that icariin and MC can jointly promote the proliferation of BMSCs and have excellent effects. On day 7, there was no significant difference in the proliferation rate of each group. This is based on the fact that the BMSCs stopped proliferating because the densities of the BMSCs at day 7 in each group were saturated. Hence, the proliferation rate showed no significant difference among the four groups. This also indicated that the AMCI/PTi scaffold had good biocompatibility.

As shown in the F-actin/DAPI staining in Fig. 3A, there were no significant differences in BMSC morphology among the four groups. In addition, the length of microfilaments was not significantly different in the CON, PTi, AMC/PTi, and AMCI/PTi groups and there was no obvious effect on BMSC morphological structure (Fig. 3C). This result further indicated the scaffold of each group had good biocompatibility.

3.4. Enhancing osteogenic ability

ALP is a specific protein in the early mineralization of the extracellular matrix and one of the functional markers for determining the phenotype of osteoblasts [39]. As shown in Fig. 4A, ALP staining was more obvious in the AMCI/PTi and AMC/PTi groups on day 7 and 10 compared with the CON and PTi groups, and the ALP staining in the AMCI/PTi group was more obvious than in the AMC/PTi group. In addition, the results of the ALP activity detection experiment showed a similar trend (Fig. 4B), and the ALP activities on day 7 of the CON, PTi, AMC/PTi, and AMCI/PTi groups were 0.85 ± 0.02, 0.86 ± 0.02, 1.04 ± 0.04, 1.33 ± 0.05 μm/mL/min, respectively. The ALP activity in the AMC/PTi and AMCI/PTi groups was significantly higher than in the CON and PTi groups, and the ALP activity in the AMCI/PTi group was significantly higher than in the AMC/PTi group. There were also significant differences between the AMCI/PTi group and the other three groups on day 10. These results indicated that both the AMCI/PTi and AMC/PTi scaffolds could promote the activity of ALP, and the addition of icariin further enhanced the activity of ALP and the osteogenic ability of the composite system. The AMCI/PTi scaffolds can significantly promote the early mineralization of the extracellular matrix by enhancing ALP activity, thereby enhancing bone regeneration.

Runx-2, a member of the Runt family of transcription factors, is one of the most important molecular factors of osteoblast differentiation and plays an important role in bone tissue formation [40]. The relative expression levels of Runx-2 were 1.03 ± 0.29, 0.78 ± 0.13, 0.76 ± 0.18, and 2.17 ± 0.58 in the CON, PTi, AMC/PTi and AMCI/PTi groups, respectively (Fig. 4C). The expression level in the AMCI/PTi group was significantly higher than in the other three groups ($p < 0.05$).

As shown in Fig. 4D, the relative expression levels of ALP in the CON, PTi, AMC/PTi, and AMCI/PTi groups were 1.01 ± 0.21, 1.01 ± 0.27, 1.57 ± 0.12, and 2.67 ± 0.34, respectively. Statistical analysis showed that the relative expression of ALP in the AMCI/PTi group was significantly higher than in the CON group ($p < 0.01$), PTi group ($p < 0.01$), and AMC/PTi group ($p < 0.01$). The relative expression of ALP in the AMC/PTi group was significantly higher than in the CON group ($p < 0.05$) and PTi group ($p < 0.05$).

OCN is a non-collagenous protein of the extracellular matrix synthesized by osteoblasts and osteocytes. Earlier studies have shown that OCN can affect bone mineral formation and mineral crystal growth [41,42]. The relative expression levels of OCN in the CON, PTi, AMC/PTi, and AMCI/PTi groups were 1.02 ± 0.24, 0.96 ± 0.30, 0.74 ± 0.06, and 1.75 ± 0.12, respectively (Fig. 4E). Statistical analysis showed that the relative expression of OCN in the AMCI/PTi group was significantly higher than in the CON ($p < 0.01$), PTi ($p < 0.05$), and AMC/PTi ($p < 0.001$) groups.

According to the above results, the activity and expression of ALP in the AMC/PTi group were significantly higher than in the CON and PTi groups. This suggested that the AMC hydrogel can promote osteogenic differentiation, and studies have shown that MC can significantly up-regulate the expression of the Wnt/β-catenin pathway *in vivo* and *in vitro* [43]. The Wnt/β-catenin pathway plays an important role in all stages of proliferation and osteogenic differentiation. In addition, MC can regulate the microenvironment of osteoblasts and enhance bone regeneration by regulating inflammation and immunity in the early stage of bone repair [44]. The ALP activity and expression of OCN, Runx-2, and ALP in the AMCI/PTi group were significantly higher than in the other three groups, suggesting that icariin and MC can synergistically promote bone regeneration. Studies have shown that icariin can induce osteoblasts to express BMP-2, BMP-4, Osx, Runx-2, ALP, and type I collagen and promote bone regeneration. Icariin can also promote the proliferation and osteogenic differentiation of BMSCs by regulating the MAPK and Wnt/β-catenin pathways [45,46].

3.5. Enhancing angiogenic ability

The effect of the AMCI/PTi scaffold on the migration and angiogenic ability of HUVECs was verified using tube formation and wound healing assays. As shown in Fig. 5A, the number of tubes in the AMCI/PTi group was significantly higher than in the other three groups. Quantitative analysis using image J showed the node numbers of the CON, PTi, AMC/PTi, and AMCI/PTi groups were 81.70 ± 7.64, 84.70 ± 9.02, 81.00 ± 8.00, and 115.00 ± 11.14 (Fig. 5C). The node number of the AMCI/PTi group was significantly higher than in the other three groups, while there was no significant difference among the CON, PTi, and AMC/PTi groups. This indicated that the AMCI/PTi scaffold can significantly promote the formation of tubes, which is conducive to vascular tissue formation. The results of the wound healing assay (Fig. 5B–D) showed that the healing areas of the CON, PTi, AMC/PTi, and AMCI/PTi groups were 12.53 ± 1.80 %, 14.99 ± 3.15 %, 11.15 ± 2.96 %, and 66.62 ± 7.17 %, respectively. The AMCI/PTi group showed significant differences compared with other groups ($p < 0.001$), but there was no significant difference among the CON, PTi, and AMC/PTi groups. This indicated that the AMCI/PTi scaffold can promote the migration of HUVECs. The above results indicated that the AMC/PTi scaffold had no significant effect on HUVECs with regard to migration and angiogenesis *in vitro*, but the addition of icariin significantly enhanced the angiogenic ability of the composite scaffold.

VEGF is a key angiogenic regulator for tube formation and the most important factor to promote angiogenesis [47]. As shown in Fig. 5E the relative expression levels of VEGF in the CON, PTi, AMC/PTi, and AMCI/PTi groups were 1.01 ± 0.21, 1.26 ± 0.03, 1.63 ± 0.98, and 3.54 ± 0.62, respectively. The statistical analysis showed that the relative expression level in the AMCI/PTi group was significantly higher than in the CON, PTi ($p < 0.01$), and AMC/PTi groups ($p < 0.05$).

HIF-1, a member of the HIF family, is able to regulate the expression of downstream target genes by inducing a locally hypoxic environment, such as VEGF and erythropoietin [48,49]. For HIF-1, the expression levels of the CON, PTi, AMC/PTi, and AMCI/PTi groups were 1.02 ± 0.25, 1.17 ± 0.34, 1.46 ± 0.57, and 3.83 ± 0.39, respectively. The relative expression in the AMCI/PTi group was significantly higher

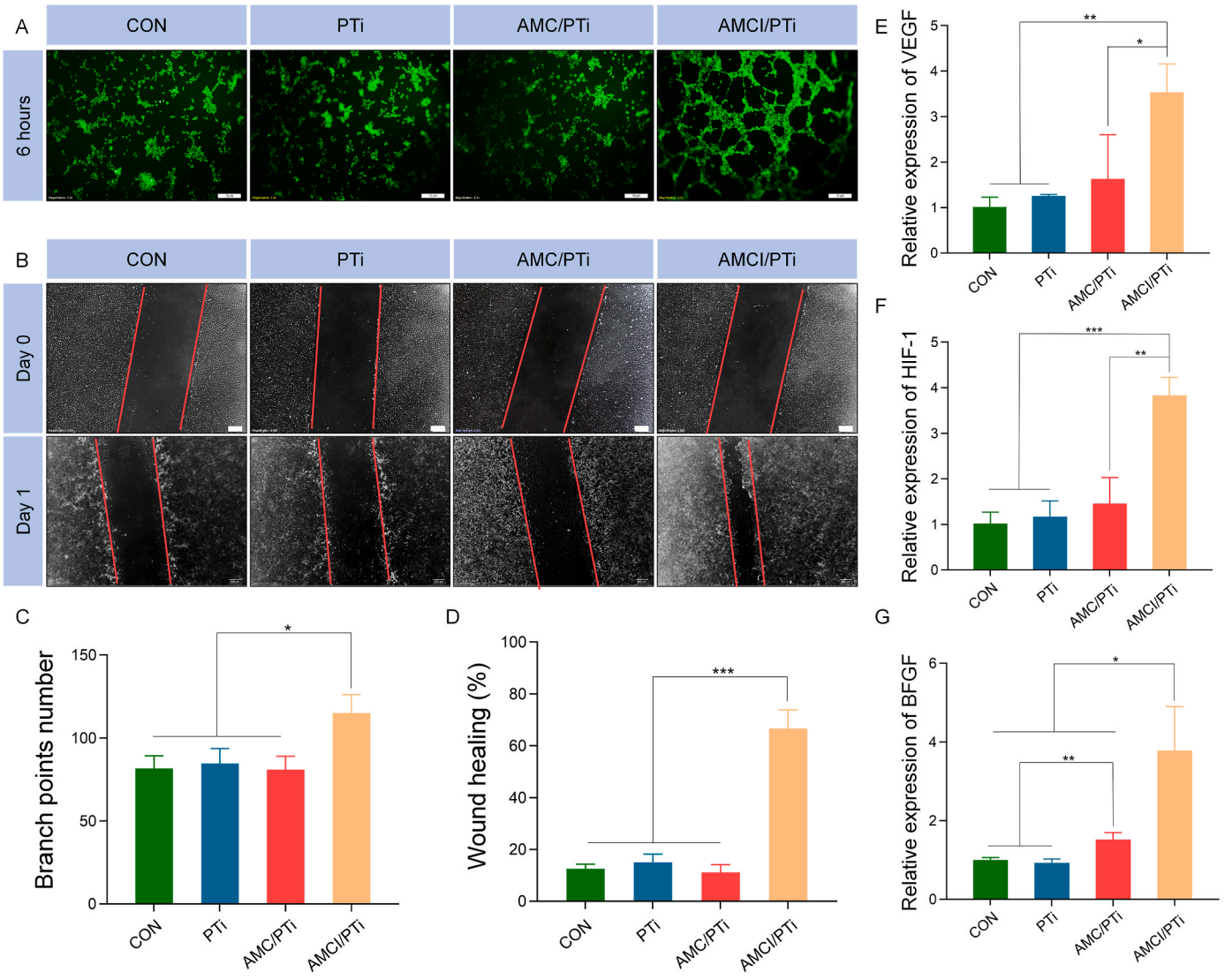

Fig. 5. The effects of each group on the migration and angiogenesis of HUVECs. (A) The images of tube formation experiment in each group after 6 h. The scale of the images was 10 μm. (B) The images of wound healing experiment after 24 h in each group. The scale of the images was 200 μm. (C) The semi-quantitative analysis of nodes in the tubule forming assay. (D) The semi-quantitative analysis of the wound healing area in each group (E, F, G). The relative mRNA expression of VEGF, BFGF, and HIF-1 in each group on day 2. (n = 3, *indicates significant differences between groups, *p < 0.05; **p < 0.01, ***p < 0.001).

compared with the CON($p < 0.001$), PTi($p < 0.001$), and AMC/PTi groups ($p < 0.01$). This indicated that although the AMC/PTi scaffold could not promote the expression of VEGF and HIF-1, the AMCI/PTi scaffold could significantly promote the expression of these genes.

BFGF is an important growth factor reported to have protective effects on the blood–brain barrier and angiogenic effects. In addition, BFGF can also promote the growth of mesenchymal and neuroectodermal cells [50]. For BFGF, the expression levels of the CON, PTi, AMC/PTi, and AMCI/PTi groups were 1.00 ± 0.06, 0.93 ± 0.09, 1.52 ± 0.18, and 3.78 ± 1.12, respectively. The relative gene expression level in the AMCI/PTi group was significantly increased compared with the CON, PTi, and AMC/PTi groups ($p < 0.05$). In addition, the relative expression level in the AMC/PTi group was significantly higher than in the CON and PTi groups ($p < 0.01$). This indicated that the AMC/PTi scaffold could promote the expression of BFGF, and the AMCI/PTi scaffold could significantly enhance BFGF expression.

There was no difference between the CON and AMC/PTi groups in the above experimental results, indicating that the AMC/PTi scaffold could not directly promote HUVEC angiogenesis and migration. According to previous studies, MC could indirectly promote angiogenesis, which was performed by regulating the immune microenvironment and inflammation [51]. There were significant differences between the AMC/PTi and AMCI/PTi groups, suggesting that the AMCI/PTi scaffold had a direct and significant effect on angiogenesis. This was because icariin can induce the expression of angiogenic factors such as VEGF and ANG1 in endothelial cells, mediate the expression of the p38/Akt pathway, and act on endothelial progenitor cells to directly promote angiogenesis [12,52]. In addition, icariin can also play a protective role in endothelial cells. Icariin can abolish hydrogen peroxide-induced apoptosis and autophagic programmed cell death in endothelial progenitor cells by reducing intracellular reactive oxygen species levels and restoring mitochondrial membrane potential levels [53]. In addition, it is worth noting that although the AMC/PTi scaffold can promote the expression of BFGF *in vitro*, it showed no obvious difference compared with the CON and PTi groups in the tube forming and wound healing assays. The reason may be that the environment was too monotonous *in vitro* since MC can promote angiogenesis through an indirect pathway *in vivo*. In conclusion, our results showed that the AMCI/PTi scaffold can significantly promote the expression of VEGF, BFGF, and HIF-1 in HUVECs and effectively enhance angiogenesis *in vitro*.

3.6. Enhanced bone defect repair

The bone defect site was detected using X-ray at 0 and 12 weeks after the operation. As shown in Fig. 6A, the scaffolds filled in the bone defect and provided stability for two ends of the bone defect. The result showed that there was bone tissue regeneration around the scaffold in each group. The scaffolds in each group were closely combined with the surrounding new bone tissue, and obvious bone ingrowth can be seen at both ends of the scaffolds. The X-ray images after surgery showed that the 3D-printed scaffolds could perfectly implant into the bone defect site, conforming to the size and shape of the bone defects (Fig. 6B). At week 12 after surgery, the AMCI/PTi scaffold was not deformed or damaged, indicating that the AMCI/PTi has a good mechanical support function and could bear the stress of the bone defect site. As a common implant in orthopedics, titanium alloy has excellent compatibility with bone tissue, and can be used as a permanent implant [54,55]. In addition, the pore structure of titanium alloy scaffold is conducive to the growth of new bone tissues [56]. This makes the scaffold-bone structure share the local stress, which can reduce the risk of scaffold damage and increase the stability of bone.

To verify the effect of the AMCI/PTi scaffold on promoting osteogenesis *in vivo*, radius samples were collected at 12 weeks after surgery for micro-CT scanning. Fig. 7A showed the CT images of the scaffold and bone regeneration inside the scaffold in each group at the radius defect site. The CT images of the three groups showed obvious bone tissue growth in all groups, and the bone tissue growth in the AMCI/PTi and AMC/PTi groups was significantly enhanced compared with the PTi group. As shown in Fig. 7B, the BV/TV values of the PTi, AMC/PTi, and AMCI/PTi groups were 1.05 ± 0.10 %, 3.80 ± 0.18 %, and 5.37 ± 0.30 %, and the BV/TV value of the AMCI/PTi group was significantly higher than in the AMC/PTi ($p < 0.01$) and PTi groups ($p < 0.001$). The BV/TV value of the AMC/PTi group was significantly higher than in the PTi group ($p < 0.05$). The Tb.Th values of the PTi, AMC/PTi, and AMCI/PTi groups were 0.07 ± 0.04 mm, 0.09 ± 0.01 mm, 0.11 ± 0.01 mm, and the Tb.Th value of the AMCI/PTi group was significantly higher than in the AMC/PTi ($p < 0.05$) and PTi groups ($p < 0.01$). The Tb.Th value of the AMC/PTi group was significantly higher than in the PTi group ($p < 0.01$). The Tb.N values of the PTi, AMC/PTi, and AMCI/PTi groups were 0.16 ± 0.02/mm, 0.36 ± 0.04/mm, 0.57 ± 0.02/mm, and the Tb.N value of the AMCI/PTi group was significantly higher than in the AMC/PTi ($p < 0.01$) and PTi groups ($p < 0.001$). The Tb.N of the AMC/PTi group was significantly higher than in the PTi group ($p < 0.01$). In addition, the differences in BMD among the three groups were consistent with those of Tb.N. In general, the Tb,N, BV/TV and BMD of AMCI/PTi and AMC/PTi were significantly higher than those of blank scaffold group, and the former is more effective. Based on the above data analysis, both the AMCI/PTi and AMC/PTi scaffolds can significantly promote bone tissue regeneration *in vivo,* and the osteogenic effect of the AMCI/PTi scaffold was significantly more obvious than that of the AMC/PTi scaffold. This was consistent with the results of *in vitro* experiments, which indicated that AMCI/PTi scaffold can also promote the repair of bone defects *in vivo*. In addition, for AMC/PTi group, MC can also promote the growth of bone tissue, but its bone repair ability was obviously insufficient because of the lack of icariin compared with AMCI/PTi group.

As shown in Fig. 8A, Masson staining and Van–Gieson staining showed there was obvious new bone regeneration at the bone defect site in the pores of the scaffolds of the PTi, AMC/PTi, and AMCI/PTi groups. Two staining results also showed the new bone area in the AMCI/PTi and AMC/PTi groups was significantly larger than in the PTi group, and

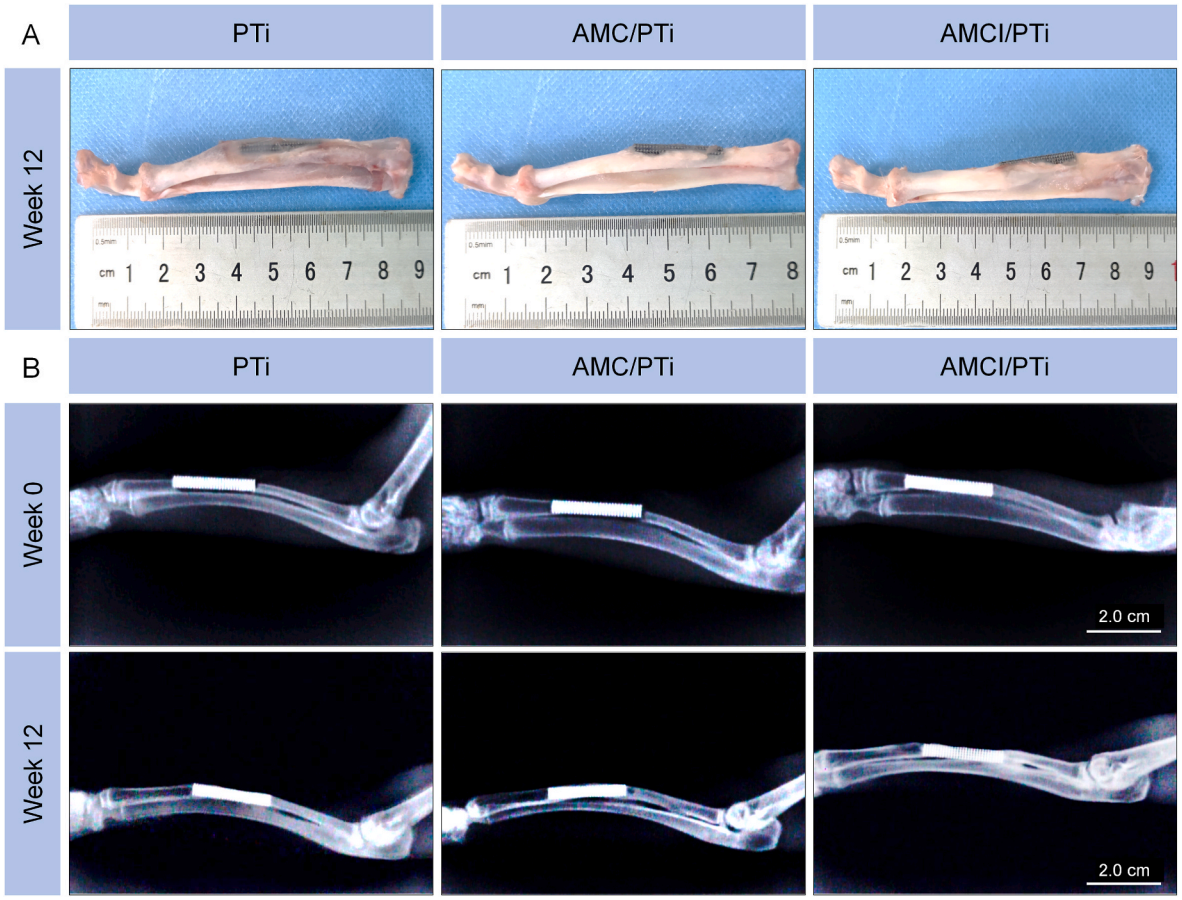

Fig. 6. The images (A) of bone defect and X-ray (B) detection at the radius defect site in each group. (The minimum scale of the ruler in the picture was 0.5 mm)

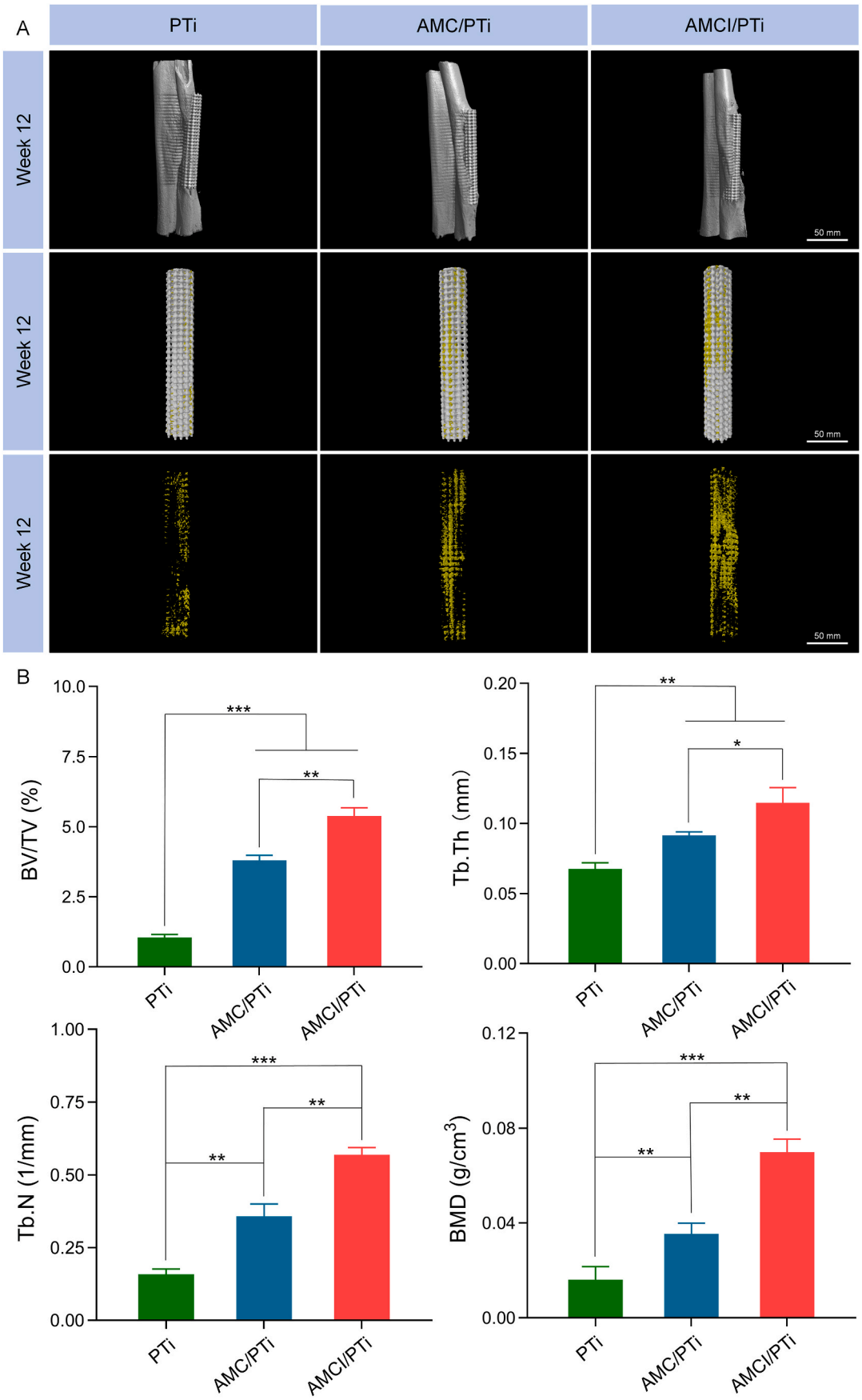

Fig. 7. The micro-CT images of each group and three-dimensional reconstruction analysis *in vivo*. (A) The 3D reconstruction analysis of each group *in vivo*. (B) The semi-quantitative analysis of bone regeneration in each group. (n = 3, *indicates significant differences between groups, *p < 0.05; **p < 0.01, ***p < 0.001).

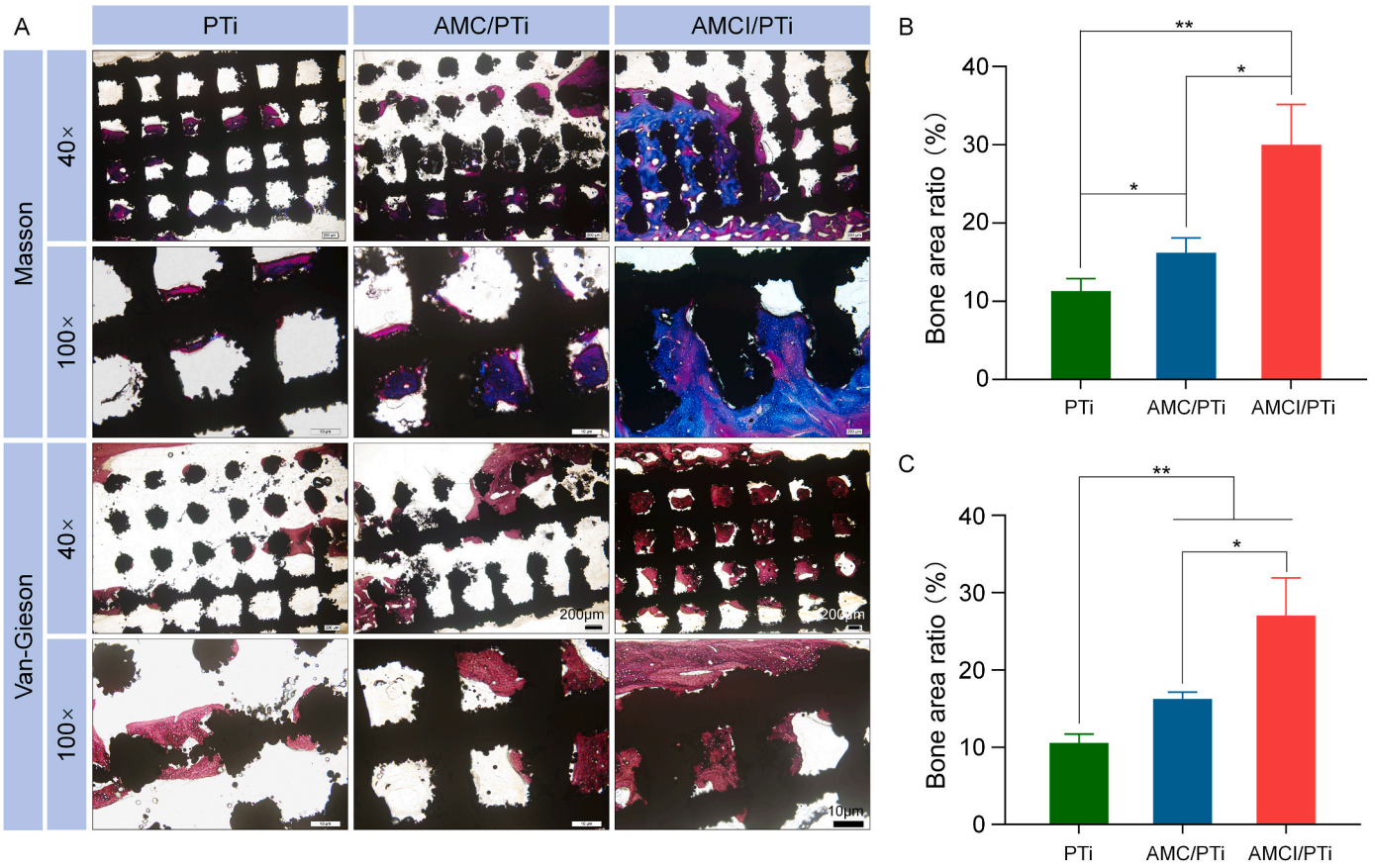

Fig. 8. Histological analysis of the bone defect site at 12 weeks after surgery. (A) Masson staining and Van–Gieson staining images of bone defects at 12 weeks after scaffold implantation (the black area was the titanium alloy, and the blue and red areas are the collagen fibers stained with Masson and Van–Gieson at the bone defect site, respectively). (B, C) The ratio of regenerated bone area to bone defect in Masson (B) and Van–Gieson (C) staining. (n = 3, * indicated significant difference between groups, *$p < 0.05$; * *$p < 0.01$).

the AMCI/PTi group was obviously larger than in the AMC/PTi group. Image J was used to analyze the effect of bone regeneration further quantitatively in each group. The bone regeneration area in the AMC/PTi and AMCI/PTi groups was significantly higher than in the PTi group ($p < 0.05$ and $p < 0.01$), and the bone regeneration area in the AMCI/PTi group was significantly higher than in AMC/PTi group ($p < 0.05$). Under Masson and Van–Gieson staining, the bone regeneration area in the AMC/PTi and AMCI/PTi groups were significantly higher than in the PTi group ($p < 0.01$), and the bone regeneration area in the AMCI/PTi group was significantly higher than in the AMC/PTi group ($p < 0.05$). Combined with the two staining results, the bone growth in AMCI/PTi group was obviously the most one, and the bone growth in AMC/PTi group was also more than that in blank scaffold group, which was also consistent with the results of micro-CT scan in Fig. 7A. This indicated that the AMC/PTi and AMCI/PTi scaffolds could promote bone regeneration *in vivo*, and the AMCI/PTi scaffold had a more significant effect. Icariin released by the AMCI/PTi scaffold in the bone defect site can promote bone regeneration and enhance the biological activity of the scaffold.

As shown in Fig. 9A, the cytoplasm of the immunohistochemical positive cells at the bone regeneration site was stained brown, and the nuclei were stained dark blue. CD31, the molecules distributed in white blood cells, endothelial cells, and platelets, not only maintain the integrity of the endothelial cells and vascular permeability but also play an important role in evaluating angiogenic molecules [57]. The CD31-positive cells in the AMC/PTi and AMCI/PTi groups were significantly increased compared with the PTi group ($p < 0.05$ and $p < 0.01$), and the AMCI/PTi group was increased significantly more than the AMC/PTi group ($p < 0.05$). In addition, the number of VEGF-positive cells in the AMC/PTi and AMCI/PTi groups was significantly higher than in the PTi group ($p < 0.01$), and the number of VEGF-positive cells in the AMCI/PTi group was increased compared with the AMC/PTi group ($p < 0.05$). The above results indicated that the AMCI/PTi scaffold can significantly up-regulate the expression of CD31 and VEGF *in vivo*, enhance local vascular circulation, and thus facilitate the repair of bone defects. In addition, although the AMC/PTi scaffold cannot promote migration and angiogenesis in HUVECs directly *in vitro*, MC can induce angiogenesis and osteogenesis as a component of bone in a previous study [58]. Therefore, MC could increase the number of CD31-positive and VEGF-positive cells through other pathways, such as regulating the immune microenvironment and inflammatory syndrome [59].

Fig. 9A and C showed that the Runx-2-positive cells in the AMC/PTi and AMCI/PTi groups were significantly higher than in the PTi group ($p < 0.05$), and the number of Runx-2-positive cells in the AMCI/PTi group was significantly higher than in the AMC/PTi group ($p < 0.01$). In addition, the number of OCN-positive cells in the AMC/PTi and AMCI/PTi groups was significantly higher than in the PTi group ($p < 0.05$ and $p < 0.01$), and the number of OCN-positive cells in the AMCI/PTi group was higher than in the AMC/PTi group ($p < 0.05$). These results indicated that the AMCI/PTi scaffold can significantly up-regulate the expression of Runx-2 and OCN *in vivo*, enhance osteogenic activity, and promote the repair of bone defects. In addition, the AMC/PTi scaffold did not show the ability to promote the expression of Runx-2 and OCN in the RT-qPCR assay, but it was found to promote the expression of both genes during the *in vivo* experiment. This indicated that although the AMC/PTi scaffold did not directly promote the expression of OCN and Runx-2 in BMSCs, it can indirectly enhance their expression through other pathways *in vivo*. Li et al. found that MC can promote bone defect

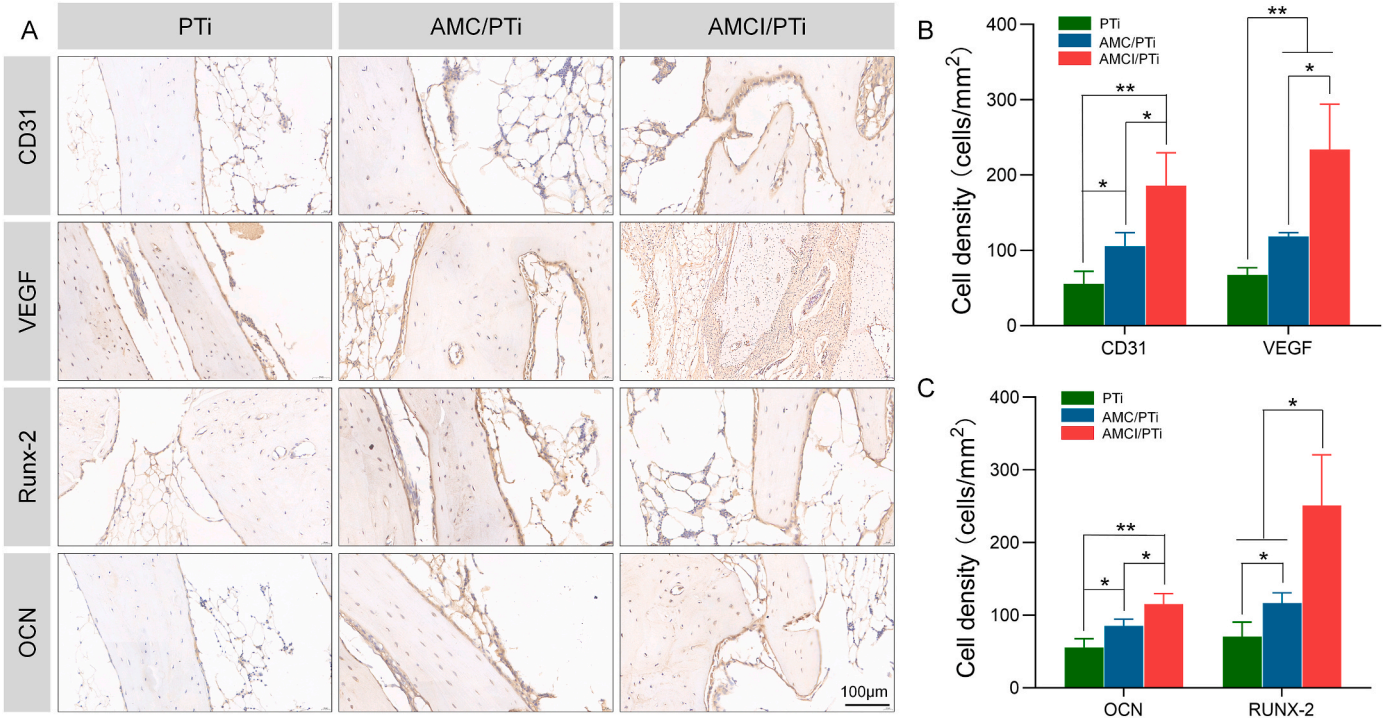

Fig. 9. Immunohistochemical analysis of the bone defect site at 12 weeks after surgery. (A) Immunohistochemical staining images of CD31, VEGF, Runx-2 and OCN antibody expression at 12 weeks after surgery. (B, C) Quantitative analysis of positive cell density per mm^2 around the new bone in scaffold pore under 400 times magnification field. (n = 3; * indicates significant difference between groups, *p < 0.05; **p < 0.01).

repair by regulating the local bone immune environment. MC of medium pore size can significantly enhance the osteogenic differentiation of MC3T3-E1 in the macrophage environment and promote the expression of OCN and ALP [60].

From the above results *in vivo* experiment, we found that the bone regeneration and angiogenesis in AMCI/PTi group and AMC/PTi group were more obvious than those in blank scaffold group, which indicated that the combination of MC and icariin can enhance the osteogenic ability and vascular regeneration ability of the system. For MC and icariin, their mechanisms for bone growth are different *in vivo*, which means that they can enhance bone repair through complementary functions. In addition, icariin can also promote the angiogenesis by promoting the expression of VEGF, BFGF and other factors. It can greatly promote the supply of nutrients and growth factors needed for early bone defect repair, and enhance the bone repair function of hydrogel system. It was very important for large segmental bone defects because of the large bone loss and serious vascular damage [61].

Based on the above results, the AMCI/PTi scaffold promoted bone repair and enhanced vascular regeneration both *in vitro* and *in vivo*, so it could be used as a good implant material for bone defect repair. The alginate/collagen ratio in the AMC hydrogel used in this study was 1:1, which confirmed that it was suitable as a bioactive material in BTE. However, one of the deficiencies of this study was that other ratios of alginate and collagen were not studied, which would be a worthy research direction in the future. According to our degradation experiment, we think that the content of collagen and HA can be reduced by increasing the proportion of alginate. This will increase the degradation ratio of hydrogel, which may have more space for the bone growth inside the scaffold. In addition, based on the excellent degradation, drug loading and release ability of AMC hydrogel, it may also perform well in combination with other therapeutic drugs for BTE.

4. Conclusion

In this study, we combined icariin-loaded AMC hydrogel with a 3D-printed titanium alloy scaffold to construct dual-functional scaffolds that can promote osteogenesis and angiogenesis. Low molecular depolymerization alginate can assist the mineralization process of collagen but also perform the loading and release of icariin. The AMCI/PTi scaffold showed suitable drug release and degradation properties *in vitro*. The scaffold was able to promote the proliferation and osteogenic differentiation of BMSCs as well as the migration of HUVECs and angiogenesis, thus facilitating bone repair of critical radius defects *in vivo*. Therefore, this study provided the critical treatment of bone defects using a promising method and offered a meaningful strategy for the construction of orthopedic bioactive scaffolds.

CRediT authorship contribution statement

Shaorong Li: Conceptualization, Data curation, Formal analysis, Funding acquisition, Writing - review & editing, Writing - original draft. **Yutao Cui:** Conceptualization, Writing - review & editing. **He Liu:** Data curation, Formal analysis. **Yuhang Tian:** Data curation, Formal analysis. **Yi Fan:** Data curation, Formal analysis. **Gan Wang:** Data curation, Formal analysis. **Jingwei Wang:** Data curation, Formal analysis. **Dankai Wu:** Conceptualization, Funding acquisition. **Yanbing Wang:** Conceptualization, Funding acquisition.

Declaration of competing interest

The authors declare that they have no known competing financial interests or personal relationships that could have appeared to influence the work reported in this paper.

Data availability

Data will be made available on request.

Acknowledgements

We thank all of the participants for their help and support. This work was supported by the 13th Five-Year Plan of Science and Technology Research of The Education Department of Jilin Province [grant number JJKH20180108KJ]; the project of Jilin Provincial Department of Science and Technology [grant number 20230402009GH]; the Industrial Technology Research and Development Project of Jilin Provincial Development and Reform Commission [grant number 2023C040-3]; and the Graduate Innovation Fund of Jilin University[41902142232R].

Appendix A. Supplementary data

Supplementary data to this article can be found online at https://doi.org/10.1016/j.mtbio.2024.100943.

References

[1] M.F. Gan, Q. Zhou, J. Ge, J.L. Zhao, Y.J. Wang, Q. Yan, C.H. Wu, H. Yu, Q. Xiao, W. X. Wang, H.L. Yang, J. Zou, Precise in-situ release of microRNA from an injectable hydrogel induces bone regeneration, Acta Biomater. 135 (2021) 289–303, https://doi.org/10.1016/j.actbio.2021.08.041.

[2] J. Li, M.X. Li, W.Z. Wang, B.H. Li, L. Liu, Evolution and development of Ilizarov technique in the treatment of infected long bone nonunion with or without bone defects, Orthop. Surg. 14 (5) (2022) 824–830, https://doi.org/10.1111/os.13218.

[3] F. Sharmin, M. O'Sullivan, S. Malinowski, J.R. Lieberman, Y. Khan, Large scale segmental bone defect healing through the combined delivery of VEGF and BMP-2 from biofunctionalized cortical allografts, J. Biomed. Mater. Res. B Appl. Biomater. 107 (4) (2019) 1002–1010, https://doi.org/10.1002/jbm.b.34193.

[4] Y.T. Cui, H. Liu, Y.H. Tian, Y. Fan, S.R. Li, G. Wang, Y.B. Wang, C.A. Peng, D.K. Wu, Dual-functional composite scaffolds for inhibiting infection and promoting bone regeneration, Mater. Today Bio. 16 (2022), https://doi.org/10.1016/j.mtbio.2022.100409.

[5] Q.L. Wang, Z.P. Huang, X. Huang, T. Zhang, W.B. Wang, Reparative effect of super active platelet combined with allogeneic bone for large bone defects, Artif. Organs 45 (10) (2021) 1219–1228, https://doi.org/10.1111/aor.14002.

[6] Y.T. Cui, T.T. Zhu, D. Li, Z.H. Li, Y. Leng, X. Ji, H. Liu, D.K. Wu, J.X. Ding, Bisphosphonate-functionalized scaffolds for enhanced bone regeneration, Adv. Healthcare Mater. 8 (23) (2019), https://doi.org/10.1002/adhm.201901073.

[7] C.L. Huang, V.P. Ness, X.C. Yang, H.L. Chen, J.B. Luo, E.B. Brown, X.P. Zhang, Spatiotemporal analyses of osteogenesis and angiogenesis via intravital imaging in cranial bone defect repair, J. Bone Miner. Res. 30 (7) (2015) 1217–1230, https://doi.org/10.1002/jbmr.2460.

[8] G. Shineh, K. Patel, M. Mobaraki, L. Tayebi, Functional approaches in promoting vascularization and angiogenesis in bone critical-sized defects via delivery of cells, growth factors, drugs, and particles, J. Funct. Biomater. 14 (2) (2023), https://doi.org/10.3390/jfb14020099.

[9] H.A. Rather, D. Jhala, R. Vasita, Dual functional approaches for osteogenesis coupled angiogenesis in bone tissue engineering, Mater. Sci. Eng., C 103 (2019), https://doi.org/10.1016/j.msec.2019.109761.

[10] Y.L. Xie, W.C. Sun, F.F. Yan, H.W. Liu, Z.M. Deng, L. Cai, Icariin-loaded porous scaffolds for bone regeneration through the regulation of the coupling process of osteogenesis and osteoclastic activity, Int. J. Nanomed. 14 (2019) 6019–6033, https://doi.org/10.2147/IJN.S203859.

[11] Y.Q. Wu, L.G. Xia, Y.N. Zhou, W.D. Ma, N. Zhang, J. Chang, K.L. Lin, Y.J. Xu, X. Q. Jiang, Evaluation of osteogenesis and angiogenesis of icariin loaded on micro/nano hybrid structured hydroxyapatite granules as a local drug delivery system for femoral defect repair, J. Mater. Chem. B 3 (24) (2015) 4871–4883, https://doi.org/10.1039/c5tb00621j.

[12] F.B. Ma, S.J. Li, L.I. Ruiz-Ortega, Y.J. Zhang, X. Lei, W. Kui, L.J. Lin, T. Bin, Effects of alginate/chondroitin sulfate-based hydrogels on bone defects healing, Mater. Sci. Eng., C 116 (2020), https://doi.org/10.1016/j.msec.2020.111217.

[13] S.T. Bendtsen, M. Wei, Synthesis and characterization of a novel injectable alginate-collagen-hydroxyapatite hydrogel for bone tissue regeneration, J. Mater. Chem. B 3 (15) (2015) 3081–3090, https://doi.org/10.1039/c5tb00072f.

[14] X.X. Li, A.H. Xu, H.G. Xie, W.T. Yu, W.Y. Xie, X.J. Ma, Preparation of low molecular weight alginate by hydrogen peroxide depolymerization for tissue engineering, Carbohydr. Polym. 79 (3) (2010) 660–664, https://doi.org/10.1016/j.carbpol.2009.09.020.

[15] Y.H. Xu, F.Y. Zhang, W.J. Zhai, S.J. Cheng, J.H. Li, Y. Wang, Unraveling of advances in 3D-printed polymer-based bone scaffolds, Polym 14 (3) (2022), https://doi.org/10.3390/polym14030566.

[16] L. Zhang, G.J. Yang, B.N. Johnson, X.F. Jia, Three-dimensional (3D) printed scaffold and material selection for bone repair, Acta Biomater. 84 (2019) 16–33, https://doi.org/10.1016/j.actbio.2018.11.039.

[17] T. Chen, Q.X. Zou, C. Du, C.R. Wang, Y. Li, B.F. Fu, Biodegradable 3D printed HA/CMCS/PDA scaffold for repairing lacunar bone defect, Mater. Sci. Eng., C 116 (2020), https://doi.org/10.1016/j.msec.2020.111148.

[18] C.Y. Zhao, H.F. Zhang, B. Cai, G.L. Wang, H.S. Fan, X.D. Zhang, Preparation of porous PLGA/Ti biphasic scaffold and osteochondral defect repair, Biomater. Sci. 1 (7) (2013) 703–710, https://doi.org/10.1039/c3bm00199g.

[19] Y. Zhao, Z.H. Wang, Y.N. Jiang, H. Liu, S.L. Song, C.Y. Wang, Z.H. Li, Z. Yang, H. Liu, J.C. Wang, B. Yang, Q. Lin, Biomimetic composite scaffolds to manipulate stem cells for aiding rheumatoid arthritis management, Adv. Funct. Mater. 29 (30) (2019), https://doi.org/10.1002/adfm.201807860.

[20] S.A. Park, H.-J. Lee, K.-S. Kim, S.J. Lee, J.-T. Lee, S.-Y. Kim, N.-H. Chang, S.-Y. Park, In vivo evaluation of 3D-printed polycaprolactone scaffold implantation combined with beta-TCP powder for alveolar bone augmentation in a beagle defect model, Mater 11 (2) (2018), https://doi.org/10.3390/ma11020238.

[21] S.Y. Fu, X.Y. Du, M. Zhu, Z.F. Tian, D.X. Wei, Y.F. Zhu, 3D printing of layered mesoporous bioactive glass/sodium alginate-sodium alginate scaffolds with controllable dual-drug release behaviors, Biomed. Mater. 14 (6) (2019), https://doi.org/10.1088/1748-605X/ab4166.

[22] Y.T. Cui, J.W. Wang, Y.H. Tian, Y. Fan, S.R. Li, G. Wang, C.A. Peng, H. Liu, D. K. Wu, Functionalized decellularized bone matrix promotes bone regeneration by releasing osteogenic peptides, Acs Biomaterials Sci. Eng. 9 (8) (2023) 4953–4968, https://doi.org/10.1021/acsbiomaterials.3c00413.

[23] C. Wang, D.L. Xu, L. Lin, S.J. Li, W.T. Hou, Y. He, L.Y. Sheng, C. Yi, X.L. Zhang, H. Y. Li, Y.M. Li, W. Zhao, D.S. Yu, Large-pore-size Ti6Al4V scaffolds with different pore structures for vascularized bone regeneration, Mater. Sci. Eng., C 131 (2021), https://doi.org/10.1016/j.msec.2021.112499.

[24] N.L. D'Elia, R.R. Silva, J. Sartuqui, D. Ercoli, J. Ruso, P. Messina, G. Mestres, Development and characterisation of bilayered periosteum-inspired composite membranes based on sodium alginate-hydroxyapatite nanoparticles, J. Colloid Interface Sci. 572 (2020) 408–420, https://doi.org/10.1016/j.jcis.2020.03.086.

[25] J.M. Gao, X.Q. Ding, X.Y. Yu, X.B. Chen, X.Y. Zhang, S.Q. Cui, J.Y. Shi, J. Chen, L. Yu, S.Y. Chen, J.D. Ding, Cell-free bilayered porous scaffolds for osteochondral regeneration fabricated by continuous 3D-printing using nascent physical hydrogel as ink, Adv. Healthcare Mater. 10 (3) (2021), https://doi.org/10.1002/adhm.202001404.

[26] A.V. Maksimkin, F.S. Senatov, K. Niaza, T. Dayyoub, S.D. Kaloshkin, Ultra-high molecular weight polyethylene/titanium-hybrid implant for bone-defect replacement, Mater 13 (13) (2020), https://doi.org/10.3390/ma13133010.

[27] D.L. Zhao, X. Wang, B. Cheng, M.M. Yin, Z.Q. Hou, X.B. Li, K. Liu, C.R. Tie, M. Yin, Degradation-kinetics-controllable and tissue-regeneration-matchable photocross-linked alginate hydrogels for bone repair, ACS Appl. Mater. Interfaces 14 (19) (2022) 21886–21905, https://doi.org/10.1021/acsami.2c01739.

[28] T.C. Ho, J.S. Park, S.Y. Kim, H. Lee, J.S. Lim, S.J. Kim, M.H. Choi, S.Y. Nam, B. S. Chun, Influences of molecular weights on physicochemical and biological properties of collagen-alginate scaffolds, Mar. Drugs 19 (2) (2021), https://doi.org/10.3390/md19020085.

[29] H. Zhu, K. Zheng, D.G. Guo, H. Zang, S. Yu, K.W. Xu, Engineering microstructure of hydroxyapatite by electron beam irradiation to induce controllable in vitro degradation, Appl. Surf. Sci. 528 (2020), https://doi.org/10.1016/j.apsusc.2020.146583.

[30] N. Saulacic, M. Fujioka-Kobayashi, Y. Kimura, A.I. Bracher, C. Zihlmann, N. P. Lang, The effect of synthetic bone graft substitutes on bone formation in rabbit calvarial defects, J. Mater. Sci. Mater. Med. 32 (1) (2021), https://doi.org/10.1007/s10856-020-06483-6.

[31] H. Zhu, K. Zheng, D.G. Guo, H. Zang, S. Yu, K.W. Xu, Engineering microstructure of hydroxyapatite by electron beam irradiation to induce controllable in vitro degradation, Appl. Surf. Sci. 528 (2020), https://doi.org/10.1016/j.apsusc.2020.146583.

[32] M.X. Lu, L.Q. Li, C.X. Zheng, Y.T. Wang, B.Q. Zhang, L. Wang, Z.Z. Li, Y.Q. Zhang, Y. Zhou, C.C. Zhou, L. Min, Y.J. Fan, C.Q. Tu, 3D printed porous PLGA/n-HA/MgP composite scaffolds with improved osteogenic and angiogenic properties, Mater, Design 234 (2023), https://doi.org/10.1016/j.matdes.2023.112351.

[33] T.L. Liu, X. Zhang, Y. Luo, Y.L. Huang, G. Wu, Slowly delivered icariin/allogeneic bone marrow-derived mesenchymal stem cells to promote the healing of calvarial critical-size bone defects, Stem Cell. Int. (2016), https://doi.org/10.1155/2016/1416047, 2016.

[34] P. Nonsuwan, K. Matsumura, Amino-carrageenan@polydopamine microcomposites as initiators for the degradation of hydrogel by near-infrared irradiation for controlled drug release, ACS Appl. Polym. Mater. 1 (2) (2019) 286–297, https://doi.org/10.1021/acsapm.8b00209.

[35] W. Su, L. Ma, Y.Q. Ran, X.M. Ma, Z. Yi, G.C. Chen, X.Y. Chen, X.D. Li, Alginate-assisted mineralization of collagen by collagen reconstitution and calcium phosphate formation, ACS Biomater. Sci. Eng. 6 (6) (2020) 3275–3286, https://doi.org/10.1021/acsbiomaterials.9b01841.

[36] H. Sun, C.X. Zhang, B.Q. Zhang, P. Song, X.J. Xu, X.Y. Gui, X.Y. Chen, G.G. Lu, X. Li, J. Liang, J.X. Sun, Q. Jiang, C.C. Zhou, Y.J. Fan, X.D. Zhou, X.D. Zhang, 3D printed calcium phosphate scaffolds with controlled release of osteogenic drugs for bone regeneration, Chem. Eng. J. 427 (2022), https://doi.org/10.1016/j.cej.2021.130961.

[37] S.Y. Qin, W. Zhou, S.Y. Liu, P.X. Chen, H.J. Wu, Icariin stimulates the proliferation of rat bone mesenchymal stem cells via ERK and p38 MAPK signaling, Int. J. Clin. Exp. Med. 8 (5) (2015) 7125–7133.

[38] Y.W. Xuan, L. Li, M.Z. Ma, J.K. Cao, Z. Zhang, Hierarchical intrafibrillarly mineralized collagen membrane promotes guided bone regeneration and regulates M2 macrophage polarization, Front. Bioeng. Biotechnol. 9 (2022), https://doi.org/10.3389/fbioe.2021.781268.

[39] S.Y. Yang, L. Wang, S.B. Feng, Q.M. Yang, B. Yu, M. Tu, Enhanced bone formation by strontium modified calcium sulfate hemihydrate in ovariectomized rat critical-size calvarial defects, Biomed. Mater. 12 (3) (2017), https://doi.org/10.1088/1748-605X/aa68bc.

[40] S.Y. Fu, H.R. Hu, J.J. Chen, Y.F. Zhu, S.C. Zhao, Silicone resin derived larnite/C scaffolds via 3D printing for potential tumor therapy and bone regeneration, Chem. Eng. J. 382 (2020), https://doi.org/10.1016/j.cej.2019.122928.
[41] O. Al Rifai, J. Chow, J. Lacombe, C. Julien, D. Faubert, D. Susan-Resiga, R. Essalmani, J.W.M. Creemers, N.G. Seidah, M. Ferron, Proprotein convertase furin regulates osteocalcin and bone endocrine function, J. Clin. Invest. 127 (11) (2017) 4104–4117, https://doi.org/10.1172/JCI93437.
[42] O. Berezovska, G. Yildirim, W.C. Budell, S. Yagerman, B. Pidhaynyy, C. Bastien, M. C.H. van der Meulen, T.L. Dowd, Osteocalcin affects bone mineral and mechanical properties in female mice, Bone 128 (2019), https://doi.org/10.1016/j.bone.2019.08.004.
[43] Z. Zhang, Z. Li, C. Zhang, J. Liu, Y. Bai, S. Li, C. Zhang, Biomimetic intrafibrillar mineralized collagen promotes bone regeneration via activation of the Wnt signaling pathway, Int. J. Nanomed. 13 (2018) 7503–7516, https://doi.org/10.2147/IJN.S172164.
[44] Y. Sun, S. Liu, Y. Fu, X.X. Kou, D.Q. He, G.N. Wang, C.C. Fu, Y. Liu, Y.H. Zhou, Mineralized collagen regulates macrophage polarization during bone regeneration, J. Biomed. Nanotechnol. 12 (11) (2016) 2029–2040, https://doi.org/10.1166/jbn.2016.2296.
[45] A.F. Yang, C.C. Yu, Q.L. Lu, H. Li, Z.H. Li, C.J. He, Mechanism of action of icariin in bone marrow mesenchymal stem cells, Stem Cell. Int. (2019), https://doi.org/10.1155/2019/5747298, 2019.
[46] Y.Q. Wu, L.G. Xia, Y.N. Zhou, Y.J. Xu, X.Q. Jiang, Icariin induces osteogenic differentiation of bone mesenchymal stem cells in a MAPK-dependent manner, Cell Prolif. 48 (3) (2015) 375–384, https://doi.org/10.1111/cpr.12185.
[47] Y.F. Liu, J. Li, J.S. Zhou, X. Liu, H.B. Li, Y. Lu, B.C. Lin, X.J. Li, T.J. Liu, Angiogenesis and functional vessel formation induced by interstitial flow and vascular endothelial growth factor using a microfluidic chip, Micromach 13 (2) (2022), https://doi.org/10.3390/mi13020225.
[48] T. Xu, X.X. Hu, G.L. Yang, Y.Y. Liu, Q. Zhang, S.Y. Yu, G.M. Chen, Y.P. Li, R. Sha, Y. S. Chen, H.Q. Xie, T.L. Guo, L. Xu, B. Zhao, HIF-1alpha/VEGF pathway mediates 1,3,6,8-tetrabromo-9 H-carbazole-induced angiogenesis: a potential vascular toxicity of an emerging contaminant, J. Hazard Mater. 432 (2022), https://doi.org/10.1016/j.jhazmat.2022.128718.
[49] M.A. Khojastehnezhad, S.M.R. Seyedi, F. Raoufi, A. Asoodeh, Association of hypoxia-inducible factor 1 expressions with prognosis role as a survival prognostic biomarker in the patients with osteosarcoma: a meta-analysis, Expert Rev. Mol. Diagn. 22 (12) (2022) 1099–1106, https://doi.org/10.1080/14737159.2022.2157719.
[50] Y. Ito, A. Oyane, M. Yasunaga, K. Hirata, M. Hirose, H. Tsurushima, Y. Ito, Y. Matsumaru, E. Ishikawa, Induction of angiogenesis and neural progenitor cells by basic fibroblast growth factor-releasing polyglycolic acid sheet following focal cerebral infarction in mice, J. Biomed. Mater. Res. 110 (12) (2022) 1964–1975, https://doi.org/10.1002/jbm.a.37434.
[51] J.Q. Shao, L.X. Weng, J. Li, H.P. Lin, H.M. Wang, J. Lin, Regulation of macrophage polarization by mineralized collagen coating to accelerate the osteogenic differentiation of mesenchymal stem cells, ACS Biomater. Sci. Eng. 8 (2) (2022) 610–619, https://doi.org/10.1021/acsbiomaterials.1c00834.
[52] D.D. Liu, Y.L. Ye, L.H. Xu, W.X. Yuan, Q. Zhang, Icariin and mesenchymal stem cells synergistically promote angiogenesis and neurogenesis after cerebral ischemia via PI3K and ERK1/2 pathways, Biomed. Pharmacother. 108 (2018) 663–669, https://doi.org/10.1016/j.biopha.2018.09.071.
[53] Y.F. Zeng, Y.L. Xiong, T. Yang, Y. Wang, J. Zeng, S.Y. Zhou, Y.M. Luo, L.S. Li, Icariin and its metabolites as potential protective phytochemicals against cardiovascular disease: from effects to molecular mechanisms, Biomed. Pharmacother. 147 (2022), https://doi.org/10.1016/j.biopha.2022.112642.
[54] X. Sun, S.D. Yang, S. Tong, S. Guo, Study on exosomes promoting the osteogenic differentiation of ADSCs in graphene porous titanium alloy scaffolds, Front. Bioeng. Biotechnol. 10 (2022), https://doi.org/10.3389/fbioe.2022.905511.
[55] H.Y. Lei, Z.G. Zhou, L. Liu, C.Y. Gao, Z.X. Su, Z. Tan, P. Feng, M. Liu, C.C. Zhou, Y. J. Fan, X.D. Zhang, Icariin-loade d 3D-printe d porous Ti6Al4V reconstruction rods for the treatment of necrotic femoral heads, Acta Biomater. 169 (2023) 625–640, https://doi.org/10.1016/j.actbio.2023.07.057.
[56] X. Pei, L.N. Wang, L.A. Wu, H.Y. Lei, P. Feng, C. Fan, Z.G. Zhou, L. Wang, M. Liu, C. C. Zhou, Q.Q. Kong, Y.J. Fan, Heterogeneous porosity design triggered stress reorganization to avoid intervertebral cage subsidence and promote spinal fusion, CmpSt 323 (2023), https://doi.org/10.1016/j.compstruct.2023.117516.
[57] L. Liu, C.X. Zheng, N. Zhao, T. Zhu, C.B. Hu, N. Zhang, J. Chen, K.C. Zhang, S. Zhang, J.X. Liu, K. Zhang, H. Jing, B.D. Sui, Y. Jin, F. Jin, Mesenchymal stem cell aggregation-released extracellular vesicles induce CD31(+)EMCN(+) vessels in skin regeneration and improve diabetic wound healing, Adv. Healthcare Mater. (2023), https://doi.org/10.1002/adhm.202300019.
[58] L.M. Ma, X.L. Wang, N.R. Zhao, Y. Zhu, Z.Y. Qiu, Q.T. Li, Y. Zhou, Z.F. Lin, X. Li, X. L. Zeng, H. Xia, S.Z. Zhong, Y. Zhang, Y.J. Wang, C.B. Mao, Integrating 3D printing and biomimetic mineralization for personalized enhanced osteogenesis, angiogenesis, and osteointegration, ACS Appl. Mater. Interfaces 10 (49) (2018) 42146–42154, https://doi.org/10.1021/acsami.8b17495.
[59] Z. Zhang, S.J. Zhang, Z.Y. Li, S. Li, J.N. Liu, C.P. Zhang, Osseointegration effect of biomimetic intrafibrillarly mineralized collagen applied simultaneously with titanium implant: a pilot in vivo study, Clin. Oral Implants Res. 30 (7) (2019) 637–648, https://doi.org/10.1111/clr.13449.
[60] J. Li, X. Luo, Z.Y. Lv, H.F. Qiang, C.Y. Hou, K. Liu, C.X. Meng, Y.J. Zhang, F.Z. Liu, B. Zhang, Microporous structures on mineralized collagen mediate osteogenesis by modulating the osteo-immune response of macrophages, Front. Bioeng. Biotechnol. 10 (2022), https://doi.org/10.3389/fbioe.2022.917655.
[61] L. Liu, F. Yu, L. Li, L.X. Zhou, T. Zhou, Y.J. Xu, K.L. Lin, B. Fang, L.G. Xia, Bone marrow stromal cells stimulated by strontium-substituted calcium silicate ceramics: release of exosomal miR-146a regulates osteogenesis and angiogenesis, Acta Biomater. 119 (2021) 444–457, https://doi.org/10.1016/j.actbio.2020.10.038.